September 1999 • NREL/SR-590-25623

Subcontractor Report

Fundamental Studies of the Effect of Crystal Defects on $CuInSe_2$/CdS Heterojunction Behavior

Final Report
28 June 1993—30 June 1998

A. Rockett
Department of Materials Science and Engineering
University of Illinois
Urbana, Illinois

National Renewable Energy Laboratory

1617 Cole Boulevard
Golden, Colorado 80401-3393

NREL is a U.S. Department of Energy Laboratory
Operated by Midwest Research Institute • Battelle • Bechtel

Contract No. DE-AC36-98-GO10337

September 1999 • NREL/SR-590-25623

Fundamental Studies of the Effect of Crystal Defects on $CuInSe_2$/CdS Heterojunction Behavior

Final Report
28 June 1993—30 June 1998

A. Rockett
Department of Materials Science and Engineering
University of Illinois
Urbana, Illinois

NREL Technical Monitor: R.D. McConnell

Prepared under Subcontract No. ZAD-3-12114-1

National Renewable Energy Laboratory

1617 Cole Boulevard
Golden, Colorado 80401-3393

NREL is a U.S. Department of Energy Laboratory
Operated by Midwest Research Institute • Battelle • Bechtel

Contract No. DE-AC36-98-GO10337

NOTICE

Available to DOE and DOE contractors from:
Office of Scientific and Technical Information (OSTI)
P.O. Box 62
Oak Ridge, TN 37831
Prices available by calling 423-576-8401

Available to the public from:
National Technical Information Service (NTIS)
U.S. Department of Commerce
5285 Port Royal Road
Springfield, VA 22161
703-605-6000 or 800-553-6847
or
DOE Information Bridge
http://www.doe.gov/bridge/home.html

 Printed on paper containing at least 50% wastepaper, including 20% postconsumer waste

TABLE OF CONTENTS

FUNDAMENTAL STUDIES OF THE EFFECT OF CRYSTAL DEFECTS ON $CuInSe_2$/CdS HETEROJUNCTION BEHAVIOR
DRAFT FINAL REPORT

A. Rockett
Department of Materials Science and Engineering
1-107 ESB, University of Illinois, 1101 W. Springfield Ave., Urbana, IL 61801

Overview:

The research program for which this is the final report was intended to address critical fundamental issues in $CuInSe_2$ (CIS) solar cell technology. The experiments focused on three major issues: 1) grain boundaries and their effects on second phase populations, bulk grain conductivity, and heterojunction behavior; 2) stoichiometry and point defects, in particular their effect on the electronic properties of bulk CIS grains; and 3) control of electronic properties and carrier collection of the heterojunction through modification of the chemistry of the CIS. The experiments involved A) growth of single crystal and polycrystalline layers as a function of thickness, composition, substrate, and growth parameters; B) testing of the structural, chemical, electronic and optical properties of the fabricated materials (including analysis of the performance of actual devices whenever possible); and C) modification of the chemistry of the deposited layers by changing the composition and microstructure of the back contact, inserting impurities directly during growth, and by post-growth heat treatment in various atmospheres.

The program was crucial to maintaining the operation of the group at the University of Illinois and in training of students. Typical staffing levels were two Ph.D. students, one visiting scientist, and two undergraduate hourlies. During this program the following personnel worked on the project and were trained in issues related to photovoltaics technologies. Ph.D. Students: Li Chung Yang (Ph.D. June, 1994), David Schroeder (Ph.D. July,97), Gene D. Berry (Ph.D. student in progress), Dong Xiang Liao (Ph.D. student in progress), Shawn O'Conner (Ph.D. student in progress). M.S. Student: John Belanger (M.S. October, 1997). Visiting Scientists and post-doc's: Gordon Kenshole (visiting scientist, United Kingdom), Hanzhong Xiao (post-doc, PRC), Jiangang Chen (post-doc, PRC), Jose Luis Hernandez (Post-doc, Spain), Karin Granath

(visiting scientist, Sweden). Undergraduate hourly research assistants: Anthony Lee (Fall '93), Anthony Minervini (Spring '94), Kristin Guilliams (Fall '94, Spring '95), Benjamin French (Summers, 1995,96,97), Terrence Yeoh (Summer, '96), Jessica Nelson (Summer, '96).

Research Approach

Many results have suggested the importance of point defects in the operation of $CuInSe_2$-based solar cells. We have addressed a number of issues in this regard during the course of this work. Details are summarized below and in more detail in the publications listed in Appendix I and in the other appendices. The studies were carried out by growth of single crystal and polycrystalline CIS of varying compositions (and hence varying point defect and grain boundary populations) by the hybrid process, developed at the University of Illinois. In addition, we have analyzed materials and devices grown at other laboratories. Additions of impurities and post-deposition treatments have been used to modify the density and electrical activity of specific point defects. The microchemical and microstructural characterizations made extensive use of the Center for Microanalysis of Materials at the University of Illinois and other facilities available to the reseach group.

The experimental details were as follows. CIGS films were deposited using a hybrid sputtering and evaporation technique from pure In and Cu magnetron sputtering sources and a Se effusion cell. In the case of the pure $CuGaSe_2$ sample the In target was replaced with a Ga target while in other samples Ga was supplied by diffusion from the GaAs substrate. The hybrid sputtering and evaporation technique. When the In target was replaced with Ga, the cooling water to that target was replaced with a recirculating water/antifreeze mixture flowing across dry ice and pumped into the target assembly. Semi-insulating (111)B-oriented GaAs wafers were used as substrates upon which $CuIn_{1-x}Ga_xSe_2$ epitaxial layers were deposited with a I/III ratio between 0.73 and 1.00, Cu/In between 0.94 and 2.04, and average Ga/(In+Ga) between 0.03 and 1.0. Cu-to-In ratios were controlled by independently varying the Cu and In target currents. A near equilibrium amount of Se was insured by using an atomic flux ratio of Se/(In+Cu)>5. Growth

temperatures ranged from 675 to 725 °C and were measured using a thermocouple calibrated with optical pyrometry. Typical film thicknesses were ~1 μm.

Compositions were determined by three techniques. To determine the average composition of the layers quantitatively, analyses were performed using a Hitachi S800 scanning electron microscope equipped with energy dispersive spectroscopy. In addition, X-ray diffraction (XRD) was conducted in a Rigaku D-Max instrument equipped with an analyzer crystal to improve resolution. Cu K-emissions were used in these measurements and, in most spectra, the contributions due to the $K_{\alpha 1}$ and $K_{\alpha 2}$ and occasionally due to the K_{β} could be observed. Finally, composition depth profiles were obtained using secondary ion mass spectrometry (SIMS) in a Cameca IMS-5f instrument.

Temperature dependent resistivity, carrier concentration, and mobility measurements were made in a diffusion-pumped cryogenic chamber using an MMR Technologies H-50 Hall Controller. Samples were contacted with ~400 nm of evaporated Au. Indium-coated Pt wires were then In-soldered to the Au pads and to In coated posts inside the cryo head. Measurements were made at temperatures between 10 and 300 K using currents between 10^{-9} and 10^{-4} A. A magnetic field of 1 Tesla was used for mobility measurements. Current was driven through different sets of contacts and in different directions for each measurement. To ensure that the GaAs wafers did not make a contribution to the electrical measurements after CIGS deposition, several wafers were measured after having the CIGS films either scraped or etched off. In all cases the underlying wafers were found to be insulating.

Results Summary:

The following results were obtained under the work funded here. Details are given in the references cited in Appendix I. Selected results are also summarized without experimental details in Appendices II-IV.

Point defects and electronic properties of $Cu(In_{1-x}Ga_x)Se_2$:

- New record results for hole mobilities in $Cu(In_{1-x}Ga_x)Se_2$ based on single crystals grown by Rockett's group. (2 conference papers, 1 J. Appl. Phys. paper)

- Demonstrated the role of Ga in determining hole concentrations. Showed that Ga does not affect the hole mobility in this material and why this is the case. Determined the diffusion coefficient for Ga in single crystal $Cu(In_{1-x}Ga_x)Se_2$. (2 conference papers, 1 Appl. Phys. Lett.)

- Demonstrated the structure and optoelectronic properties of the $CuIn_3Se_5$ ordered-defect phase of $CuInSe_2$. (1 J. Appl. Phys. paper)

- Characterized the detailed effects of Na on $Cu(In_{1-x}Ga_x)Se_2$ solar cells and on the fundamental properties of the material itself (reduces compensating donors in p-type materials). (3 conference papers, 1 J. Appl. Phys.)

- In collaboration with groups at the Universities of Salford and Liverpool in the United Kingdom, studied the effect of ion implantation damage on $Cu(In_{1-x}Ga_x)Se_2$ single crystals. (3 conference papers, 1 Phil Mag.)

Materials for and characterization of devices:

- Developed a novel contact metallurgy which improves adhesion to the underlying Mo back contact in solar cells made with $Cu(In_{1-x}Ga_x)Se_2$. This material has also yielded substantial novel materials science behaviors including grain rotation and growth prior to phase separation in a metastable binary alloy. (1 patent, 1 Scripta Met and 2 J. Appl. Phys. papers, 2 conference papers)

- Characterized the electroluminescence as a function of temperature and Ga content in $Cu(In_{1-x}Ga_x)Se_2$ solar cells and shown that the radiative recombination pathways are not band-to-band as in normal semiconductors but rather proceed through defect states. (1 conference paper, 1 Masters thesis).

- Working with a group at the University of Uppsala in Sweden, have demonstrated novel aspects of the bonding and chemistry of dip coated CdS heterojunction materials used as heterojunction partner materials in $Cu(In_{1-x}Ga_x)Se_2$ solar cells (1 conference paper, 1 Solid State Phenom.)

Other work:

- Principal author on one review article on $Cu(In_{1-x}Ga_x)Se_2$ (Thin Solid Films). Co-author on a second review article (Solar Energy Materials and Cells).

Additional work has been carried out as part of the CIS Mo Team effort under the program described here. The work was conducted in collaboration with K. Granath (Uppsala Univeristy), S. Asher, M. El Jassim, Hasoon, R. Matson, (NREL), B. Basol (ISET), J. Britt (EPV), and T. Gillespie (Lockheed Martin Corporation). This work has not been completed and published but has been reported at CIS Team meetings. The work demonstrates that Na concentration in CIGS is related to grain structure. In addition, single crystals of CIGS grown by the group have been distributed to other research groups for testing and analysis. The results of these analyses are described in papers P9, P10, C1, and C2 listed in Appendix I. Details of results in these papers are not summarized here due to space constraints but may be found in the cited works.

APPENDIX I

Papers Published During this Project:

Papers published in archival journals:

P1. A. Rockett, F.Abou-Elfotouh, D. Albin, M. Bode, J. Ermer, R. Klenk, T. Lommasson, T.W.F. Russell, R.D. Tomlinson, J. Tuttle, L. Stolt, T. Walter, and T.M. Peterson, "Structure and Chemistry of $CuInSe_2$ for Solar Cell Technology: Current Understanding and Recommendations", Thin Solid Films **237**, 1 (1994).

P2. L. Chung Yang and A. Rockett, "Cu-Mo Contacts to $CuInSe_2$ For Improved Adhesion in Photovoltaic Devices," J. Appl. Phys **75**(2), 1185 (1994).

P3. H. Xiao, L.-Chung Yang, and A. Rockett, "Structural, Optical and Electrical Properties of Epitaxial Chalcopyrite $CuIn_3Se_5$ Films," J. Appl. Phys. **76(3)** 1503 (1 August 1994).

P4.J.R. Tuttle, J.R. Sites, A. Delahoy, W. Shafarman, B. Basol, S. Fonash, J. Gray, R. Menner, J. Phillips, A. Rockett, J. Scofield, F. Shapiro, P. Singh, V. Suntharalingam, D. Tarrant, T. Walter, S. Wiedeman, and T.M. Peterson, "Characterization and Modeling of $Cu(In,Ga)(S,Se)_2$-Based Photovoltaic Devices: A Laboratory and Industrial Perspective", Progress in Photovoltaics **3**, 89 (1995).

P5. L.-Chung Yang, H. Xiao and A. Rockett, W. N. Shafarman and R.W. Birkmire, "The Fabrication of Device-quality Bilayer $CuInSe_2$ Films by the Hybrid Sputtering and Evaporation Method", Solar Energy Materials & Cells **36(4)** 445-455 (1995).

P6. H.Z. Xiao, L.-Chung Yang, S.L. Lai, Z. Ma, and A. Rockett, "Structural Properties of Metastable Cu-Mo Solid Solution Thin Films Synthesized by Magnetron Sputtering", Scripta Metallurgica et Materialia, **32(3)** 353-358 (1995).

P7.G. Ramanath, H.Z. Xiao, L.C. Yang, A. Rockett, and L.H. Allen, "Evolution of Microstructure in Nanocrystalline Mo-Cu Thin Films During Thermal Annealing", J. Appl. Phys. **78**(4), 2435 (1995).

P8. David J. Schroeder, Gene D. Berry, and A. Rockett, "Gallium Diffusion and Diffusivity in $CuInSe_2$ Epitaxial Layers", Applied Physics Letters, **69** (26), 1 (1996).

P9. C.A. Mullan, C.J. Kiely, M.V. Yakushev, M. Imanieh, R.D. Tomlinson, and A. Rockett, "The Effects of Ion Implantation on the Microstructure of $CuInSe_2$ Single Crystals", Phil. Mag. A. **73**(4), 1131-1145 (1996).

P10. A.J. Nelson, G. Berry, A. Rockett, D.K. Shuh, J.A. Carlisle, D.G. Sutherland, L.J. Terminello, "Observation of Core-level Binding Energy Shifts Between (100) Surface and Bulk Atoms of Epitaxial $CuInSe_2$", J. Appl. Phys. **70(14)**, 1873-5 (1997).

P11. David J. Schroeder and Angus A. Rockett, "Electronic Effects of Sodium in Epitaxial $CuIn_{1-x}Ga_xSe_2$", J. Appl. Phys. **82(10)**, 4982 (1997).

P12. David J. Schroeder, Jose Luis Hernandez, Gene D. Berry and Angus A. Rockett, "Hole Transport and Doping States in Epitaxial $CuIn_{1-x}Ga_xSe_2$", J. Appl. Phys. **83(3)**, 1519 (1998).

Papers published in Conference Proceedings:

C1. C.A. Mullan, C.J. Kiely, M. Imanieh, R.D. Tomlinson, and A. Rockett, "Ion Implantation Effects in Single Crystal $CuInSe_2$", Inst. Phys. Conf. Ser. **134**, 547 (1993).

C2. C.A. Mullan, C.J. Kiely, L.Chung Yang, and A. Rockett, "Electron Microscopy Studies of Epitaxial $CuInSe_2$ Layers Grown on GaAs by a Hybrid Magnetron Sputtering Process", Inst. of Phys. Conf. Ser. **138**, 305 (1993).

C3. L. Chung Yang, G. Berry, H.-Z. Xiao, and A. Rockett, "Structure and Optoelectronic Properties of Single Crystal Epitaxial $CuIn_{1-x}Ga_xSe_2$ and Ordered Defect Compounds", Proceedings of the First World Conference on Photovoltaic Energy Conversion, 5-9 Dec, 1994, Waikoloa, Hawaii (Institute of Electrical and Electronics Engineers, New York, 1995) 172.

C4. J.L. Hernández and A. Rockett, "JUNCTION ELECTROLUMINISCENCE OF $Cu(In,Ga)Se_2$ DEVICES", 25th IEEE Photovoltaic Specialists Conference, Washington D.C., May , 1996 (Institute of Electrical and Electronics Engineers, New York, 1996), 973.

C5. Angus Rockett, M Bodegård, Karin Granath and Lars Stolt, "Na Incorporation and Diffusion in $CuIn_{1-x}Ga_xSe_2$", 25th IEEE Photovoltaic Specialists Conference, Washington D.C., May , 1996 (Institute of Electrical and Electronics Engineers, New York, 1996), 985.

C6. A. Kylner, A. Rockett, and L. Stolt, "Oxygen in Solution Grown CdS Films for Thin Film Solar Cells," Diffus. Defect Data B, Solid State Phenom **51**, 533-9 (1996).

C7. A. Rockett, R. Birkmire, D. Morel, S. Fonash, J-Y. Hou, M. Marudachalam, J. D'Amico, P. Panse, S. Zafar, and D.J. Schroeder, "Next Generation CIGS for Solar Cells", Proceedings of the Future Generation Photovoltaic Technologies Meeting, Inst. Phys. Conf. Ser. in press.

C8. David J. Schroeder, Jose Luis Hernandez, and Angus A. Rockett, "Point Defects and Hole Transport in Epitaxial $CuIn_{1-x}Ga_xSe_2$", Proceedings of the 11th International Conference on Ternary and Multinary Compounds (8-12 Sept., 1997), Inst. Phys. Conf. Ser. in press.

APPENDIX II

Defects & Electronic Properties of $Cu(In_{1-x}Ga_x)Se_2$

II.A. Structure and Properties of the $CuIn_3Se_5$ Ordered Defect Compound

This section summarizes the results of publications P3 and C3 listed in Appendix I. These form the first and remain the most complete study of single crystal $CuIn_3Se_5$. The single crystal $CuIn_3Se_5$ layers investigated in this study were deposited directly on (001)-oriented GaAs wafers. The cathodoluminescence (CL) system used in this study is based on a Zeiss scanning electron microscope (SEM) and employs a Ge detector and a liquid-He cooled stage for low temperature measurements (≥4.3 K). Optical absorption, transmission, and reflection measurements were carried out at room temperature using a Perkin Elmer Lambda-9 double beam spectrometer equipped with an integrating sphere. Absorption coefficients were calculated from the transmission and reflection measurements. Film resistivities were measured by the four-point probe technique at room temperature after dismounting the substrates from the Mo sample blocks and removing the excess In from the back surface. Surface morphologies and compositions of the epitaxial layers were examined using a Hitachi S-800 SEM equipped with an energy dispersive X-ray spectroscopy (EDS) system. Standard specimens with a known composition were used to quantify the EDS data in determining the film compositions. Microstructural studies (electron diffraction and bright- and dark-field imaging analyses) were carried out in Philips EM420 and CM12 transmission electron microscopes (TEMs). High resolution TEM studies were performed using a Hitachi 9000 TEM operated at 300 kV. Plan-view and cross-sectional TEM samples were prepared by mechanical thinning to 50-80 μm and then ion milled to perforation on a (77 K) cold stage using 3 kV Ar^+ ions. The plan-view samples were thinned from the GaAs substrate side to minimize damage to the films.

SEM electron channeling patterns indicated that single crystal (002)-oriented epitaxial films rippled anisotropically along <110> with an (001) surface orientation were obtained on GaAs(001). No evidence of grain boundaries was found. EDS measurements showed that the

epitaxial films had an overall composition of 11 at.% Cu, 33 at.% In, and 56 at.% Se, indicating that the film was $CuIn_3Se_5$ to within the accuracy of the EDS analysis.

Optical transmission and reflection data were recorded as a function of wavelength and photon energy and an absorption coefficient was determined from these, see Fig. II.A.1a. The absorption coefficient α was ~$5x10^3$ cm^{-1} at 1.25 eV and $2x10^4$ cm^{-1} at 1.4 eV. Values for photon energies above ~1.43 eV were unmeasurable due to absorption in the GaAs. The absorption coefficient decreased exponentially [i.e.: $\alpha=\alpha_o e^{-E/\eta}$ where α_o is a proportionality constant] with photon energy E below ~1.4 eV with a characteristic energy η of ~85±10 meV. The decrease in absorption was much slower than typically observed for CIS and suggests the presence of band tails participating in absorption. This suggestion was supported by CL measurements. A typical CL spectrum is given in Fig. II.A.1b. Spectra recorded as a function of position on the sample showed no significant variations in emission properties as a function of position, indicating no large optically active defects in the film. As shown in Fig. II.A.1b, a photon emission peak occurred at an energy of ~1.18 eV. The peak is very broad and decreases nearly exponentially from an energy just below the maximum to ~0.9 eV. The characteristic slope of this decrease is 75±5 meV. This suggests that CL photon emission below the peak resulted from radiative recombination between the defect states rather than between the conduction and the valence bands. Epitaxial layers had resistivities of $>10^5$ Ω-cm. Dislocations, antiphase domain boundaries, stacking faults and nanotwins were observed by TEM in the epitaxial layers. Typical plan-view dark-field TEM micrographs indicating these defects are shown in Fig. II.A.2. The micrograph in Fig. II.A.2a was formed using the (200) superlattice reflection and shows the anti-phase domain boundaries associated with stacking faults. Fig. II.A.2b is a weak beam dark-field image obtained under the g(3g) condition (where g was the (220) diffraction vector used to form the image and 3g satisfies the Bragg condition). Dislocations labeled by arrow heads and stacking fault and nanotwin fringes can be seen. High resolution micrographs of stacking faults and nanotwins, obtained from cross-sectional specimens with the $[1\,\bar{1}\,0]$ orientation, are presented in Fig. II.A.3. Two stacking faults (Fig. II.A.3a), indicated by arrows, formed on the (112) plane

at a separation of six (112) atomic plane spacings. [Note that six (112) plane spacings is the minimum necessary to span a complete tetragonal chalcopyrite unit cell.] Nanotwins on the {112} planes, such as the one marked by T in Fig. II.A.3b with boundaries indicated by arrows, were also common. The (001) surface of the $CuIn_3Se_5$ was rippled, converting the surface to more stable $\{112\}_{Se}$ planes. Formation of twins and stacking faults is common during vapor phase growth on these (close-packed) planes. Adatoms can be accommodated at several possible sites without disturbing the nearest neighbor bonds; thus, growth accidents, especially at high growth rates (>1μm/hour), can result in twin and stacking fault formation. However, these defects are common in polycrystalline materials used for devices and apparently do not cause major loss of performance in the resulting devices. This is also in agreement with the lack of contrast in CL intensity or spectrum as a function of position on the sample surface.

Stacking faults, anti-phase domain boundaries, and nanotwins were removed by rapid thermal annealing (RTA) in a gaseous nitrogen environment. The sample was heated at ~150°C/sec to a temperature of 700°C, held at this temperature for 60 seconds, and then cooled by radiation cooling to room temperatures (over a few seconds). During RTA the dislocation density was found to increase, as demonstrated in bright-field plan view (Fig. II.A.4) and cross sectional TEM images. Selected area electron diffraction patterns (SADPs) formed using a large (30 μm) aperture showed no evidence of unit cell orientation domain boundaries after RTA.

SADP's were obtained from the epitaxial layers in a number of zone axes. Numerous reflections were observed which are forbidden in an ideal chalcopyrite structure, as listed in Table II.A.I. (100), (010), and (110) diffraction points in the [001] zone-axis patterns are due to ordered point defects resulting from the deviation of $CuIn_3Se_5$ from an ideal chalcopyrite structure, see Fig. II.A.5a and b. The {101} and {103} reflections in the [001] zone-axis patterns are superlattice points from domains in which the unit cell is rotated with respect to the predominant epitaxial relationship given above, as shown in Fig II.A.5c. Extra diffraction spots produced by stacking faults and nanotwins result in: streaks along the $(11\bar{2})$ and $(1\bar{1}2)$ diffraction vectors in the [021] zone-axis pattern in Fig. II.A.6; $(\bar{2}\,\bar{2}8)/3$, $(\bar{2}4\bar{4})/3$, and $(4\bar{2}\,\bar{4})/3$ in the [221] zone axis;

$(\bar{4}\,\bar{2}\,\bar{4})/3$, $(24\bar{4})/3$, and $(2\,\bar{2}8)/3$ in the $[\bar{2}21]$ zone axis; $(\bar{4}\,\bar{2}4)/3$, $(224)/3$, and $(2\,\bar{2}\,\bar{8})/3$ in the $[2\,\bar{2}1]$ zone axis; and $(\bar{2}44)/3$, $(\bar{2}\,\bar{2}\,\bar{8})/3$, and $(4\,\bar{2}4)/3$ in the $[22\,\bar{1}]$ zone axis. Typical examples of these zone-axis patterns are presented in Fig. II.A.7. The assignment of these reflections to specific defects is discussed and justified in the following paragraphs.

Electron diffraction patterns from the as deposited epitaxial $CuIn_3Se_5$, Fig. II.A.5, confirmed that $CuIn_3Se_5$ is a defect-ordered chalcopyrite compound in the epitaxial layers. Figure II.A.5a is a [001] zone-axis pattern including (100), (010), and (110) diffraction points, which are forbidden in the chalcopyrite structure. A computer simulated [001] zone-axis pattern is shown in Fig. II.A.5b. In the simulation, ordered In on Cu site antisite defects (In_{Cu}) were introduced on the (001) plane of the chalcopyrite structure. In_{Cu} defects have been estimated to have the lowest formation energy, 1.4 eV, of the common point defects in $CuInSe_2$ and account, in part, for the difference in stoichiometry of the deposited layer with respect to $CuInSe_2$. The replacement of Cu^+ ions by In^{+++} ions creates net positive charges in the lattice that can be balanced by adding Se^{--} ions or Cu^+ vacancies to maintain the charge neutrality. Cu vacancies are thought to have lower formation energies than Se point defects and contribute to the change in overall stoichiometry. The In_{Cu} defect is believed to produce a shallow donor and the V_{Cu} defect a shallow acceptor. When present in equal numbers, these defects cause no change in net valence and consequently no uncompensated donor or acceptor states are introduced into the solid. This accounts for the very high film resistivity ($>10^5$ Ω-cm) observed. The In_{Cu} donor level is thought to lie 35-45 meV below the conduction band edge and the V_{Cu} shallow acceptor level is thought to lie 30-45 meV above the valence band edge.

TEM analyses showed that the majority of as-deposited epitaxial layers were aligned with [001] parallel to the [001] substrate direction. Occasional rotated domains with [100] or [010] parallel to the GaAs[001] were also observed. Diffraction spots of {101}- and {103}-types, labeled by arrow heads in Fig. II.A.5a, are superlattice reflections from these rotated domains. The simulated diffraction pattern of Fig. II.A.5c including the three orientations but without ordered point defects in the crystal agrees well with the pattern in Fig. II.A.5a and confirms that the (010),

(001), and (012) reflections are point-defect derived. Fig. II.A.8a is a high resolution TEM micrograph taken along the [001] orientation from a plan-view sample. Two domains, present in the micrograph and marked by D1 and D2, respectively, were aligned perpendicularly. The boundary between these domains is irregular and labeled by arrow heads. A blurred image around the domain boundary and a distorted lattice image in D1 can be seen in Fig. II.A.8a. The blurring can be attributed to the lattice mismatch (0.3 %) between the domains due to the tetragonal distortion of the chalcopyrite unit cell. In addition to the preferred orientation relationship, $CuIn_3Se_5$(001)//GaAs(001) and $CuIn_3Se_5$[110]//GaAs[110], electron diffraction patterns, Figures 8(b) and 8(c), obtained from the [100]-oriented domains show GaAs(001)//$CuIn_3Se_5$(100) and GaAs[110]//$CuIn_3Se_5$[021], or GaAs(001)//$CuIn_3Se_5$(010) and GaAs[110]//$CuIn_3Se_5$[201].

Zone-axis patterns with [021] and [221] orientations are shown in Fig's II.A.6 and II.A.7, respectively. In the [021] zone, (012)- and (100)-type forbidden reflections produced by the ordered point defects and streaking along the $(11\bar{2})$ and $(1\bar{1}2)$ diffraction vectors can be seen. The streaks resulted from planar defects formed on the {112}-type planes, such as the stacking faults and nanotwins. Reciprocal rods or diffraction streaks produced by the {112}-type stacking faults in the faulted $CuIn_3Se_5$ appear along the <221> directions, or along the {112}-type diffractions in the reciprocal space, as shown in Fig. II.A.6. Due to their finite thickness, the intensity distribution of the nanotwins at reciprocal lattice points is increased in the <221> directions, resulting in the streak formation along the {112}-type diffractions as well. Stacking fault- and nanotwin-induced streaking in the diffraction patterns was removed by RTA, as shown in the [021] zone-axis SADP, Fig. II.A.9a.

Experimental (a) and computer simulated (b) diffraction patterns with a [221] zone axis are shown in Figure II.A.7. In addition to $(0\bar{1}2)$-, $(\bar{1}02)$-, $(1\bar{2}2)$-, and $(\bar{2}12)$-type forbidden spots caused by the ordering of the defects, $(4\bar{2}\bar{4})/3$-, $(\bar{2}4\bar{4})/3$-, and $(\bar{2}\,\bar{2}8)/3$-type extra reflections are present and are marked by arrow heads in Fig. II.A.7a. These extra reflections result from stacking faults and nanotwins and were removed by RTA [see for example, Fig. II.A.9b obtained after RTA].

Conclusions

The single crystal $CuIn_3Se_5$ epitaxial films exhibit a defect-ordered microstructure and an energy band gap of at least 1.18 eV with significant density of states in the gap, probably distributed in band tails near the two band edges. The density of states near the Fermi energy is small in this film, and the defect states in the material are highly compensated. This suggests that the states giving rise to the sub-gap absorption and luminescence are distributed as approximately symmetric band tails. The ordered defects in this material can locally reduce the energy gap even below the gap of ideal $CuInSe_2$. The modified band structure of the defect ordered compound and the line and planar defects reported here apparently do not degrade device performances. Anti-phase domain boundaries, stacking faults, and nanotwins were also common in the $CuIn_3Se_5$ epitaxial layers. RTA was found to eliminate the planar defects from the films at the cost of introduction of additional dislocations.

II.B. Hole Mobilities in $Cu(In_{1-x}Ga_x)Se_2$

This section summarizes portions of the results of publication P12 listed in Appendix I. This work reports and describes processes limiting the highest mobilities in p-type $Cu(In_{1-x}Ga_x)Se_2$ observed to date.

Carrier concentrations and Hall mobilities were measured as a function of temperature in single crystal epitaxial layers grown on GaAs substrates. Values were calculated from resistivities and Hall voltages using standard equations. The Hall scattering factor was assumed to be equal to 1 across the entire temperature range**.** The true Hall scattering factor may vary from unity. This may lead to an overestimation of the true drift mobility and underestimation of the hole concentration by as much as a factor of two near room temperature.

II.B.i. Temperature Dependent Hole Concentration

Figures II.B.1a and II.B.1b show the experimental and calculated carrier concentrations, as a function of inverse temperature, for samples without and with a Ga gradient, respectively. Samples without a Ga gradient span much of the Ga composition range while those without a gradient have low Ga contents. Fig II.B.1a illustrates samples with low (CIS T0) and high (CIS 135) levels of compensation at higher and a relatively uniform but moderate Ga concentration and two samples with higher Ga content (CIS 25 having 56 % Ga and CGS 5 being pure $CuGaSe_2$). Fig II.B.1b shows the three general ranges of compensation (high for CIS 68, medium for CIS 61, and low for CIS T1) for three samples including a Ga gradient. We note the general similarity in the curves in Figs II.B.1a and II.B.1b which indicates that the Ga gradient does not appear to be affecting the general behavior of the samples. The steep slope at high temperatures and a shallower slope at low temperatures, is indicative of two acceptor levels with the acceptors responsible for the steeper slope having a larger concentration than the acceptors responsible for the shallower slope.

Fits to these data were achieved by considering the two acceptor levels apparent in Figure II.B.1 and compensating donors that are expected to be present in this material. Fits to the data considering either fewer or additional acceptor states produced unacceptable matches to the data. Because of compensation and the two acceptor defect levels, the relevant charge neutrality condition becomes [1]

$$p = \left(N_{A_1} - n_{A_1}\right) + \left(N_{A_2} - n_{A_2}\right) - N_D \qquad \text{(II.B.4)}$$

where, N_{A_i} is the total number of acceptors at an energy level i, n_{A_i} is the number of acceptors at level i which are not ionized, and N_D is the total number of donors. All donors are assumed to be ionized. From this the following expression for carrier concentration can be obtained [1]

$$p = N_{A_1}\left[\frac{1}{1+g_{a_1}\exp\left(\frac{E_{A_1}-E_F}{kT}\right)}\right]+N_{A_2}\left[\frac{1}{1+g_{a_2}\exp\left(\frac{E_{A_2}-E_F}{kT}\right)}\right]-N_D, \qquad \text{(II.B.5)}$$

$$\text{where } \exp\left(\frac{E_A-E_F}{kT}\right)=\frac{p}{N_V}\exp\left(\frac{E_A-E_V}{kT}\right), \qquad \text{(II.B.6)}$$

E_A, E_F, E_V are the acceptor, Fermi, and valence band edge energies, respectively, k is the Boltzmann constant and T is the temperature in Kelvin. The degeneracy factor for acceptors, g_a, is a ratio $g_a=\frac{g_a^-}{g_a^o}$ where g_a^- is the number of unique configurations in which a hole can reside in the valence band and g_a^o is the number of unique configurations in which a hole can reside on the acceptor states.[2] Because CIS has both heavy and light hole valence bands and a hole may be spin up or down, g_a^-=4. If the acceptor states are assumed to be hydrogenic single acceptors then there is only one possible configuration for a hole occupying them so g_a^o=1 and g_a=4. For purposes of fitting this data several different values of g_{a_1} and g_{a_2} were tried. It was found that these parameters primarily affected estimates of the acceptor state densities N_{A_1} and N_{A_2}. The fitted parameter values given in Table I were calculated assuming g_{a_1}=2 (divalent acceptors) and g_{a_2}=4 which are consistent with the assignment of these states given later in this paper. Combining equations II.B.5 and II.B.6 while letting

$$X=\frac{g_{a_1}}{N_V}\exp\left(\frac{E_{A_1}-E_V}{kT}\right) \qquad \text{(II.B.7)}$$

$$\text{and } Y=\frac{g_{a_2}}{N_V}\exp\left(\frac{E_{A_2}-E_V}{kT}\right) \qquad \text{(II.B.8)}$$

yields the following cubic expression for the hole concentration p:

$$XYp^3 + \left(X + Y + XYN_D\right)p^2 + \left(1 - YN_{A_1} - XN_{A_2} + XN_D + YN_D\right)p + N_D - N_{A_1} - N_{A_2} = 0. \quad \text{(II.B.9)}$$

Equation II.B.9 was the final form with which the data in Figures II.B.1a and II.B.1b and similar data for other samples, not shown, were fitted.

Closer inspection of Figure II.B.1b reveals that fits to the carrier concentration at low temperatures fall below the measured concentration of carriers and the sample labeled CIS T1 shows an apparent increase in carrier concentration with decreasing temperature. This behavior indicates the presence of hopping conduction that is most likely occurring in the shallower of the two impurity states. This conduction is expected to increase with an increasing density of impurity states and with increasing compensation, since at sufficiently low temperature the only charge carriers available in this state must be supplied by compensating donors. In all cases $N_{A_1} + N_{A_2} > p >> N_D$ at room temperature and in many cases $N_{A_2} > N_D$.

One significant trend is revealed as function of composition. As Ga content is increased both of the acceptor defect densities are found to increase. This is shown in Figure II.B.2. It should be noted that at room temperature the hole concentrations of several samples are high enough that some error in the fits may result as the condition $(E_F\text{-}E_V)\geq 3kT$ is violated.

Although the data is noisy, the depth of both the shallow and deep acceptor states decrease approximately logarithmically with increasing number of states. This is as expected if isolated states are at constant depth and the observed depth change results only from broadening of the impurity band. A best fit to the data presented in Table II.B.I suggests a decrease in depth of 7 and 12 meV for the shallow and deep states, respectively, per decade of change in acceptor density. This behavior suggests that the defe-genic as they appear to remain roughly fixed with respect to the band edge as the alloy composition changes. In turn, this indicates that errors due to changes in Ga content within a film should have been small as no energy difference in the valence band, causing holes to move, would result.

II.B.iii. Temperature Dependent Hole Mobility

Figures II.B.3a and II.B.3b show the measured Hall mobility for the same samples as in Figures II.B.1a and II.B.1b. These samples (and all others studied for this work) exhibit very similar near-room-temperature behaviors as well as peaks in their mobility vs. temperature curves.

Mobility results were fit to obtain a qualitative understanding of how transport in these films changes, or does not change, as a function of composition. It was not possible to obtain exact quantitative estimates of physical parameters. However, adequate fits were generally obtained using parametric values in agreement with previous studies. Table I lists the fitting parameters necessary for calculating Hall mobilities and carrier concentrations for all samples. Other parameters that were not varied include:[3,4] high frequency dielectric constant (8.1), static dielectric constant (13.6), hole effective mass (0.73), Debye temperature (395 K), velocity of sound (2.2×10^5 cm/s), density (5.77 g/cm^3). A comparison between the fitting parameters and composition does not show any clear trends. However, rough correlations exist between the concentrations of acceptors, donors, and the temperature at which the peak in mobility occurs. Because values for these parameters were not available for $CuGaSe_2$, the same values were used in modeling all films.

$CuInSe_2$ has hybridized p-d valence band wave functions. Standard theories describing scattering were derived assuming s-like wave functions. Thus the existing theories cannot be expected to predict correct quantitative values for mobility in CIGS. However, corrections to the theory for holes with p-like wave functions in III-V compounds have been developed, and the temperature dependencies of the mobility remain unchanged.[5] Therefore, it may be reasonable to expect that the temperature dependencies will again remain unchanged in the case of holes in hybridized p-d wave functions. This is especially true since the Cu d-orbitals affect primarily the lower valence band. Also, it is expected that the absolute value of the mobility will more closely approximate the value for holes in III-V materials than that of electrons with s-like wave functions. Therefore, in fitting experimental data, equations were used which include corrections for holes in

p-like wave functions, when available. It was also assumed that the temperature dependence of mobility is consistent between III-V materials and $CuInSe_2$.

Further complications include the fact that all of the samples measured here contain at least some Ga which changes the band structure and therefore the transport behavior of the resulting films. Because the Hall effect measures the majority carrier behavior, then if the depth of isolated acceptor states does not change significantly with Ga content, the band edge is probably not changing with respect to the Fermi level and no field will be present in the material. If the scattering mechanisms in pure $CuInSe_2$ and pure $CuGaSe_2$ do not change, then there should be no effect on the data due to a Ga gradient in the film. A comparison of results for the pure $CuGaSe_2$ sample and samples containing very little Ga [Ga/In+Ga <0.05] shows that after accounting for the change in acceptor state density there is no change in the depth of the acceptor state and there is no change in the predominant scattering mechanisms. This indicates that a Ga concentration gradient should have no effect on *majority* carrier behavior in agreement with results on samples containing a substantial Ga gradient.

Hall mobility data fits considered acoustic and non-polar optical phonon scattering, polar optical phonon scattering, neutral impurity scattering, and ionized impurity scattering. The approximate total mobility was calculated using Matthiessen's rule [5]

$$\frac{1}{\mu_{total}} \approx \frac{1}{\mu_{PO}^{eff}} + \frac{1}{\mu_{AC,NPO}} + \frac{1}{\mu_n} + \frac{1}{\mu_{II}^{eff}}. \qquad \text{(II.B.10)}$$

where μ_{total}, μ^{eff}_{PO}, $\mu_{AC,NPO}$, μ_n, and μ^{eff}_{II} are the total hole mobility and mobilities limited by polar-optical, acoustic and non-polar optical, neutral impurity and ionized impurity scattering mechanisms, respectively. The equations governing the individual scattering mechanisms were from Wiley, [5] with the exception of scattering by neutral impurities which is given by Erginsoy.[6]

Figure II.B.4 shows the experimental and calculated mobility limited by the above mechanisms vs. temperature for a typical sample. It can be seen in this figure that while non-polar

optical and acoustic phonons appear consistent with the near room temperature mobility, polar optical phonons underestimate this mobility. This underestimation is consistent in all samples and therefore scattering due to polar optical phonons was removed from Equation II.B.10. Similar changes have been found necessary in modeling of p-type III-V semiconductors.[5] Because the mobility vs. temperature is nearly flat at the peak over a large temperature range in many samples it appears that the limiting mobility is due to the presence of neutral impurities. However, poor fits to the mobility data were obtained assuming that the neutral defect population resulted from the same defects which caused the donors and acceptors. When a constant value of ~$5x10^{17}$ cm^{-3} was used for the neutral defect concentration, good fits to all samples were possible. Because this value does not change significantly from sample to sample, we believe that this is not due to an extended defect such as dislocations whose density varies significantly from sample to sample. We propose that the clustered point defects which form due to deviations in stoichiometry dominate scattering in this temperature regime.

The slope of the mobility with temperature at temperatures below the peak is far too steep to be explained by ionized impurity scattering but is consistent with the onset of hopping conduction.[1,5]

II.B.iv. Hopping Conduction

In an effort to confirm the presence of hopping conduction and that the onset of hopping conduction is related to the defect densities observed in the carrier concentration vs. temperature data, fits were carried out which included conduction due to carriers in the valence band and carriers which are hopping between acceptor states. It was assumed that the contribution to the Hall voltage for *electrons* moving by hopping conduction is negative and that the combined conduction occurs by a simple parallel conduction path model. This yields a Hall coefficient: [1]

$$R_H = \frac{r\left[p - \left(\frac{\mu_{hop}}{\mu_{VB}}\right)^2 N_A^{2-}\right]}{q\left[p + \left(\frac{\mu_{hop}}{\mu_{VB}}\right) N_A^{2-}\right]^2} \qquad \text{(II.B.11)}$$

where μ_{VB} is the valence band mobility and the mobility of hopping carriers is assumed to be given by: [7]

$$\mu_{hop} = \mu_{hop}^{o} \exp\left(-\left(\frac{\varepsilon_{hop}}{kT}\right)^{\frac{1}{4}}\right). \qquad \text{(II.B.12)}$$

Assuming that the constant μ_{hop}^{o} will be inversely proportional to the exponential of the average spacing between states and proportional to the fractional occupancy of these states,[II.B.25]

$$\mu_{hop}^{o} = C f_{N_{A_2}} \exp\left(N_{A_2}^{1/3}\right). \qquad \text{(II.B.13)}$$

$N_{A_2}^{-}$ is the number of acceptors in the shallower level which are ionized (from fitting p(T) data with Equation II.B.5), ε_{hop} is the characteristic hopping conduction energy, $f_{N_{A_2}}$ is the fraction of unionized shallow acceptors (from p(T) fits), and C is a constant. Figure II.B.5 shows fits to the mobility vs. temperature curves for two samples where ε_{hop} was taken to be 1 meV. Good agreement with the temperature at which mobility drops sharply was obtained using these parameters for all samples with incompletely compensated N_{A_2} states. It is apparent, however, that the transition from normal to hopping conduction predicts a more abrupt transition than was observed. This may be due to local variability in the density of N_{A_2} states in the epitaxial layers. Also, it is not well understood what the magnitude, or even the sign of the Hall coefficient should be for carriers moving by a hopping conduction mechanism. Samples in which very high levels of compensation completely filled the shallower impurity state did not fit well with Equations

II.B.11-13 using the same values of ε_{hop} and C. However, the general qualitative behavior of these samples was quite similar to the less compensated results. The hopping conduction in the highly compensated samples presumably occurs in the deeper states and may require modification of ε_{hop} and C to obtain good fits.

II.B.v. DISCUSSION

The I/III ratios of all samples indicate that they are far from stoichiometric $Cu(In_xGa_{1-x})Se_2$. Therefore, large numbers of In_{Cu}^{++}, Ga_{Cu}^{++} and V_{Cu}^{-} defects are expected to compensate for the deviations from stoichiometry. If all of the defects responsible for deviations in stoichiometry were electrically active (that is, each contributing a donor or acceptor state) the samples would have been heavily compensated and the acceptor and donor concentrations would have been well over 10^{21} cm^3. Clustering of point defects which are responsible for deviations from stoichiometry is one possible explanation for their being electrically inactive. For example, with a deviation of only 1% in stoichiometry, a random spacing between oppositely charged defects is sufficiently small (according to a simple hydrogenic model and if distributed to minimize local net charge) to push most of the states out of the bandgap.[2] This makes the assignment of defect levels extremely difficult from experimental data. It seems from the lack of dependence on I/III ratio that the electrically active defects may not be ones which would normally be thought of as being responsible for deviations from stoichiometry in these materials. That is, simply because the samples are known to be group III rich does not necessarily mean that In_{Cu}^{++}, Ga_{Cu}^{++} or V_{Cu}^{-} defects are the dominant electrically active defects. This argument leaves Cu_{In}, V_{Cu}, or V_{In} as potential low formation energy intrinsic sources of the observed acceptor states.

On the basis of on energy of formation estimates, we suggest that Cu_{In} defects may account for the deeper, higher concentration, acceptor defect, while the shallower, lower-density defect may be due to vacancies on one of the metal sublattices. If these assignments are correct, it is expected that there should be another acceptor level caused by Cu_{In}^{--} which should be near the intrinsic level in energy and have a density which is approximately equal to the room temperature

carrier concentration. While the hydrogenic model probably does not apply, such a behavior would be consistent with divalent substitutional defects in other semiconductors. For example, doubly ionized states are two to three times deeper for divalent substitutional elements in Si and Ge than are the singly ionized states. This may explain the suggestion of such a near mid-gap level present at high concentrations based on modeling of operating devices.[8]

Because of the much lower compensation density found in these samples compared to other epitaxial layers some explanation for the levels reported here seems necessary. The most likely cause of this behavior seems to be that in the growth technique used for the production of these samples (and standard device-quality polycrystals) a large excess of Se is present throughout the deposition and also during sample cooling. This excess Se should have reduced the number of Se vacancies which are likely to be the source of electron donors in this material. Another possibility is that the higher growth temperature used in this study allowed for a greater motion of point defects and enhanced the ability of defects to cluster. It seems likely that the variability in the compensation of our samples is a result of variation in the cooling rate and Se pressure during cooling which may have been modified by changes in thermal contact to the sample holder or slight changes in sample geometry. We can find no other experimental explanation for the variability of the results.

The data for high Ga-content alloys and pure $CuGaSe_2$ shows that addition of Ga causes the acceptor concentration to increase to values closer to the number of majority point defects in the material. These results imply that the addition of Ga increases acceptor density by changing either the energy associated with the formation of metal vacancies or the ease with which defects are able to cluster and form complexes which push their states out of the bandgap. We believe that the most probable explanation is due to changes in the clustering of defects.

CONCLUSIONS

Observations described here confirm the basic conclusions of previous works such as the presence of an ~150 meV-deep acceptor state. Unlike in previous works, the density of this state

does not change significantly with film composition other than with Ga content (see next section for a description). This difference with respect to previous works may have resulted from the high Se activity during growth of all layers. The films grown for this study have a much lower compensation level than previously reported which allowed observation of a lower concentration shallower acceptor. Fitting the data also allowed determination of the concentration of a compensating donor state. We find that the mobility near room temperature and the peak mobility are not substantially influenced by the film composition or acceptor state density including being unaffected by Ga content or by a Ga gradient. The room temperature mobility is determined by phonon scattering as found by previous studies. The peak mobility, when not limited by hopping conduction, is limited by neutral impurity scattering although this does not appear to be correlated with the number of states contributing to electrically active donor and acceptor populations. Both the room temperature and peak mobilities are higher than previously observed.

II.C. The Effect of Ga on $Cu(In_{1-x}Ga_x)Se_2$

This section summarizes the results of publications P8 and portions of P12 listed in Appendix I.

Figure II.C.1 shows the Ga^+ count rate from secondary ion mass spectrometry (SIMS) normalized to the Ga signal in the GaAs substrate for several samples with different Cu/In ratios. The substrate/film interface was defined where the Ga signal had dropped by 40%. Total depths were determined by microprofilometry measurements of the craters. Samples with Cu/In ratios deviating significantly from 1.0 have nearly flat profiles, while those with Cu/In ratios near 1.0 exhibit error-function-like behaviors. Because of the tendency of GaAs to remain stoichiometric it is not possible to deplete the GaAs substrates of Ga. Therefore, the Ga concentration in the GaAs remains constant. All of the Ga in the films was found to come from Kirkendall voids which formed in the GaAs during CIGS growth, see Figure II.C.2. Kirkendall void size was found to correspond to the total Ga content of the films. Thus, the supply of Ga to the film is not limited by

bulk diffusion of Ga in GaAs, but rather by the decomposition reaction of GaAs with a lattice vacancy expanding the void.

To quantify these results, numerical solutions (using a forward difference approximation) of Fick's Second Law including surface Ga loss and film growth were carried out. Three boundary conditions were assumed: 1) the Ga concentration is constant at the GaAs/CIS interface, 2) the film growth rate is constant, and 3) loss of Ga at the surface to the vacuum is controlled by some rate constant k_{loss}. These boundary conditions yielded the following forward difference equations:

$$c_0^n = c_0^{n+1} \tag{1}$$

for the GaAs/CIGS interface,

$$c_k^n = c_k^{n+1}\left(1 + 2\frac{D\Delta t}{\Delta x^2}\right) - \frac{D\Delta t}{\Delta x^2}\left(c_{k+1}^{n+1} + c_{k-1}^{n+1}\right) \tag{2}$$

for typical nodes, and

$$c_{surface}^n = c_{surface}^{n+1}\left(1 + \frac{D\Delta t}{\Delta x^2} + k_{loss}\frac{\Delta t}{\Delta x}\right) - \frac{D\Delta t}{\Delta x^2}c_{surface-1}^{n+1} \tag{3}$$

at the surface of the film. These were then solved using a successive overrelaxation procedure with a time step of 1 second. Best fits were obtained by using $k_{loss} = 0$ for all samples, indicating that Ga desorption to the vacuum was negligible. Figure II.C.3 shows the fit to the experimental SIMS data for two samples obtained using the above procedure.

Figures II.C.1 and II.C.3 both show a discontinuity at the GaAs/CIGS interface. The measured magnitude of this discontinuity vs. Cu/In ratio, see Figure II.C.4, decreases as the Cu/In ratio increases. We propose that there are differences in the stability of Ga atoms on Cu compared to In vacancies and specifically that Ga atoms favor In sites. Therefore Cu-rich films would be able to accomodate Ga more readily as they contain more In vacancies. This, in turn, increases the Ga content in the CIGS near the interface and hence decreases the discontinuity.

Except in the pure $CuGaSe_2$, Ga diffused into the films from the GaAs substrates during sample growth. The Ga profiles were nearly flat (change in Ga content front to back of less than 20%) for all films with Cu/In ratios greater than 1.05. Profiles in films with Cu/In≈1 followed a

complimentary error function behavior with changes in Ga content front to back of as much as a factor of 50. Diffusion of Ga into $CuInSe_2$ layers grown on GaAs has also been observed by Yang II.C.5 and by Fons et al. II.C.18 The SIMS measurements of Ga content were calibrated by XRD. A typical XRD spectrum and mixed Gaussian-Lorentzian curve fit for film CIS 152 are shown in Fig. II.C.5. The main film doublet in the XRD data was used to determine the predominant Ga content of the layer. Average Ga contents were also checked by energy dispersive spectroscopy and found to be in good agreement with XRD for films with uniform Ga contents. XRD spectra showed strong GaAs (111) $K_{\alpha 1}$-$K_{\alpha 2}$ doublets as well as one or more sets of peaks due to the CIGS film. The typical intensity resulting from the CIGS included a sharp (0.03° half-width at half maximum) doublet due to the predominant composition in the film along with a broad background due to changes in the Ga concentration near the substrate. It is interesting to note that the minority composition shoulder did not generally extend beyond the GaAs peak. This suggests that strain had a strong effect on Ga out diffusion near the CIGS/GaAs interface preventing Ga compositions with lattice constants smaller than GaAs. This supports the conclusions of Fons et.al. concerning strain-driven interdiffusion. II.C.18

Figure II.C.6 shows the diffusivity of Ga in CIS at 725°C vs. Cu/In ratio. From this, it can be seen that the diffusivity of Ga is a strong function of CIS composition, being minimized just below a Cu/In ratio of 1.0. This is consistent with the idea that the number of vacancies on the metal sublattices should be minimized near Cu/In=1.0. The presence of Kirkendall voids also supports Ga diffusing by a vacancy mechanism. Cu-rich films are generally thought to include large numbers of In vacancies while In-rich films include many Cu vacancies. Thus, the steep increase in diffusivity on either side of the minimum indicates that Ga is able to diffuse by a vacancy mechanism through either Cu or In vacancies. We note that it is reasonable to expect a vacancy diffusion mechanism because $CuInSe_2$ and $CuGaSe_2$ are miscible at least to 25% Ga. This implies that Ga is readily accommodated on lattice sites in CIS. The somewhat smaller diffusivity on the In - rich side of the minimum may be the result of the energy penalty

associated with Ga occupying Cu sites compared to In sites, consistent with the above interpretation of the interfacial discontinuity.

It was surprising to find that even films deposited with very high Cu/In ratios, became Ga+In (group III)-rich. That is, diffusion of Ga was sufficient to make very In poor films group III rich. All films had compositions with I/III<0.8. Cu/In and I/III ratios for films studied here are given in Table II.C.I. One possible cause of this is that once the film reaches a stoichiometric I/III ratio of 1.0 any metal vacancy which forms thermally will be filled by a Ga atom, the only available type of atom. In the event that this is an indium vacancy the Cu/(In+Ga) ratio is maintained. In the event that it is a copper vacany a Ga atom may still occupy this position forming a Ga_{Cu}^{+} defect which in turn will cause the production of more V_{Cu}^{-} defects to maintain charge neutrality. This process would push the I/III ratio below 1.0..

The diffusivities obtained here are in reasonable agreement with results obtained for In diffusion in polycrystalline $CuInSe_2$ | $CuGaSe_2$ diffusion couples, which yielded diffusivities of between $3x10^{-13}$ and $5x10^{-12}$ cm^2/s at temperatures between 400 and 600 °C.[9] This suggests that diffusion in polycrystals is intragranular rather than intergranular. The diffusivity of Ga in CIS was found to vary between $2.7x10^{-13}$ and $5x10^{-11}$ cm^2/s in this study at a single temperature of 725 °C, depending upon composition. This range of diffusivity is significantly larger than the range found in polycrystalline CIS between 400 and 600 °C and indicates that the film composition is a more important factor than is temperature in controlling the diffusivity of Ga in CIS.

Finally, we note that the mechanisms controlling the interfacial discontinuity and the diffusivity are probably different. Transport of Ga atoms through the CIGS film is kinetically limited as determined by the diffusivity while the discontinuity is limited by an equilibrium between vacancies in the CIGS which occur in high concentrations and Ga atoms from the GaAs on the vacant sites. Thus, the two processes are independent and have different behaviors as a function of composition.

II.D. The Effect of Na on $Cu(In_{1-x}Ga_x)Se_2$

This section summarizes the results of publications P11 and C5 listed in Appendix I. The addition of Na to CIGS devices, either by diffusion from these substrates or intentionally added as Na_2Se before the deposition process, has been found to enhance device performance. The mechanism behind device improvement by Na has been widely debated. At least two groups have found evidence of enhanced grain growth, increased (112) texturing and an increase in device performance when Na was present in the films.[10,11] Another study indicated that Na decreases resistivity as well as the activation barrier to conduction in the plane of polycrystalline thin film CIGS.[12] This behavior was attributed to a decrease in the potential barrier to conduction across grain boundaries. Still others have found that Na increases the open-circuit voltage of polycrystalline devices and reduces depletion width.[13] The suggested explanation in this case was that Na acted to increase effective hole concentration by neutralizing donor Se vacancies through an enhanced chemisorption of oxygen in the presence of Na. Na has also been linked to the appearance of an acceptor state 75 meV above the valence band in device layers.[14] The papers in this section describe the mechanisms for introduction of Na into polycrystalline CIGS (section i) and its electronic effects (ii).

II.D.i. Diffusion of Na into CIGS Polycrystalline Layers

This section summarizes the results of publication C5 listed in Appendix I. CIGS used for this work was deposited by coevaporation from resistively heated open boat sources with mass spectrometer control of the Cu, In, and Ga fluxes at Uppsala University. Three types of Mo-coated substrates were used, soda-lime glass with and without an Al_2O_3 diffusion barrier, and sintered Al_2O_3. The Mo back contact material was rf-diode sputtered to a thickness of ~0.5 μm in ultrahigh purity Ar. X-ray photoelectron spectroscopy measurements of the Mo layers showed up to 10 atomic percent concentrations of oxygen in the form of MoO_2 and MoO_3. Two of the samples (CIGS/Mo/uncoated Na-lime glass and CIGS/Mo/Al_2O_3) were implanted with Na^+ at 60

keV energy to a dose of $1x10^{15}$ cm^{-3}. After SIMS analysis to characterize the as-implanted samples, each was annealed in an ultrahigh vacuum furnace having a base pressure of ~10^{-8} Torr.

As-implanted CIGS layers showed well-defined implant peaks (see Fig. II.D.i.1) as well as Na in the bulk of the films and in the Mo back contacts. The Na in the CIGS grown on Mo on Al_2O_3 resulted primarily from the implant while the Na in the sample on Mo on Na-lime glass resulted mostly from diffusion out of the substrate through the Mo layer. The relative smoothness of the Na concentration in the CIGS layer on Na-lime glass shows that the Na diffusivity in CIGS is high at the growth temperature. No diffusion of Na in the implants was observed at room temperature, even after six months.

The SIMS profiles in Fig. II.D.i.1 indicate a measurable amount of Na in the Mo back contact for substrates both with and without Na. Changes in the Na ion yield in Mo and CIGS could affect the profiles and give a false impression of the Na concentration in the Mo. To avoid this, the relative yields in Mo and CIGS were determined explicitly by ion implanting a Mo layer and measuring the resulting profile. Based on comparisons of the measured profiles for the implants it was determined that the ion yield of Na in Mo is ~2.5 times smaller than in the CIGS. This indicates that the Na concentration is actually higher in the Mo after correction for SIMS effects than appears in the profiles in Fig. II.D.i.1.

From this analysis, it can be concluded that segregation of Na from the CIGS into the Mo occurs. This resutls in an equilibrium change in Na concentration across the CIGS/Mo interface of a factor of ~100 at the CIGS growth temperature. Similar segregation behaviors were observed in samples grown on other substrates and in typical device quality layers without implants.

After characterization of the samples as-implanted, a vacuum anneal was carried out in which the temperature was increased to 420°C over 20 minutes, maintained constant for an additional 20 minutes, and cooled rapidly to room temperature. Following the annealing step the samples were reanalyzed by SIMS. A comparison of the implants in the CIGS on Mo on Na-lime glass sample before and after annealing is given in Fig. II.D.i.2.

Annealing this sample resulted in no significant change in the concentration of Na in the bulk of the layer. However, much of the implant peak disappeared. The base concentation of Na in the annealed sample shown above (~$8x10^{18}$ cm^{-3}) is consistent with the previous bulk concentration throughout the layer (see Fig. II.D.i.1). The diffusion increased the Na concentration gradient near the surface which is indicative of a segregation behavior.

A similar motion of Na out of the CIGS was observed for the sample on Mo on Al_2O_3 as shown in Fig. II.D.i.3 but the diffusion proceeded further until after annealing the implant was no longer visible and the Na profile in the sample reached an equilibrium level. Because this anneal was conducted at a lower temperature (420°C) than the original CIGS growth, the segregation ratio for Na in CIGS and Mo is reduced to approximately a factor of 10.

The diffusion of the Na implant toward the surface at 420°C suggests that Na motion is rapid both in the grains and in the grain boundaries in the CIGS. The implant inserts Na into both the grains and the boundaries. Hence, for the implant profile to disappear, Na in both locations must move. Furthermore, the apparant motion of Na to the film surface must be different from simple motion of Na out of grains to the grain boundaries which would not necessarily move the implant profile as the Na might move laterally rather than in depth. The observed motion represents a change in depth of the implant.

The remaining question is where the Na in the CIGS layer is located. This is significantly more difficult to determine because atomic imaging of Na in grains and grain boundaries is not feasible. However, SIMS ion images were obtained for the samples and showed the presence of Na-rich regions at locations where low In and Cu signals were obtained. This was also true in Cu-rich samples where ion images in some cases showed Na-rich areas in addition to Cu-rich second phase regions but not at the same locations. However, in many images there was no evidence of Na-rich areas. The imaging results suggest that when Na is present in high enough concentrations it may cluster into intergranular precipitate phases (of undetermined composition). At lower concentrations it is roughly uniformly distributed.

The tendency of Na to segregate out of CIGS to the sample surface was confirmed by XPS. Device quality layers having high Na contents (detectable by XPS) were examined and shown to have significant (atomic percent) Na concentrations on their surfaces. The samples were then rinsed in deionized water, dried and returned to the XPS system. No Na was detected on the surfaces. However, upon heating to ~300°C the Na reappeared on the surface. This cycle could be repeated and was observed reproducibly for different samples.

CONCLUSIONS

We conclude that Na segregates rapidly out of CIGS at normal physical vapor deposition temperatures. No Na diffusion at room temperature was observed in samples after six months. The segregation drives Na both to the surface of polycrystalline layers and into the Mo substrate. The segregation ratio for the CIGS/Mo interface is ~ 10 at 400 °C and ~100 at 600°C. Small Na-rich regions can also occur inside CIGS layers. In spite of these observations, Na leads to a strong (112) preferred orientation of CIGS and apparantly improves the performance of devices.

II.D.ii. The Electronic Effects of Na on CIGS

This section summarizes the results of publications P11 listed in Appendix I. Definitive proof of the mechanism by which Na acts in CIGS has been lacking. Existing studies have been particularly complicated by the presence of grain boundaries. This study, therefore, determined the effects of Na on the electronic properties of epitaxial single crystal CIGS.

For this work, as deposited epitaxial films were cleaved and the surfaces of the films were coated with Na from either evaporated Na_2Se or solution deposited NaOH. The samples were then annealed in vacuum to diffuse the Na into the CIGS. Exact annealing conditions for this step for the samples tested are given in Table II.D.ii.I. The Na surface layers were then rinsed off with deionized water and the samples were annealed again for 15 minutes at 550 °C to drive the Na into the entire film and thus to flatten out the Na profile. This second anneal was performed on all samples. Both Na-coated and uncoated control samples were put through identical annealing and

rinsing cycles to insure that any measured differences were the result of the presence of Na and not other processing.

Figures II.D.ii.1 and II.D.ii.2 show SIMS profiles of Na concentration and O^-/Se^- ratios, respectively, for the sample with and without NaOH treatment after the completion of annealing. Table II.D.ii.I gives Na concentrations for all samples measured. Only slight, factor of < 5, differences in O concentration were observed for the samples coated with NaOH while the Na concentration was found to change by a factor of nearly 100. Samples treated with Na_2Se showed no significant change in O concentration. Figure II.D.ii.3 shows the experimentally determined and calculated carrier concentrations as a function of inverse temperature for a sample contaminated with Na using a NaOH solution and the uncontaminated control sample. The behavior seen in Figure II.D.ii.3, a steep slope at high temperatures and a shallower slope at low temperatures, is consistent with the presence of two acceptor levels with the acceptors responsible for the steeper slope having a larger concentration than the acceptors responsible for the shallower slope. This two acceptor level behavior is typical of the behavior seen in these samples without intentional contamination (see Section II.B., above). The rise in apparent carrier concentration at very low temperatures in one of these samples is due to the onset of hopping conduction which causes Hall voltage and mobility to drop while resistivity remains nearly constant as temperature is decreased. Fits to the data were achieved by considering the two acceptor levels apparent in Figure II.D.ii.3 and the compensating donors which are expected to be present in this material. The exact fitting procedure is given in detail with all relevant equations in Ref. 10. The fitting parameters for all samples are given in Table II.D.ii.II. The fitting of this data generally allowed estimates of acceptor level densities and activation energies as well as the density of compensating donors to be obtained. In cases where the shallower of the two acceptor defects was completely obscured by a high level of compensation the depth and density of the shallow acceptor was assumed to be equal to the value found for a less compensated (Na contaminated) piece of the same sample. We believe that this is a reasonable assumption because a number of samples have been found which

exhibit the shallower acceptor level without intentional (or accidental as verified by SIMS) Na contamination.

The primary difference between the Na-treated and untreated samples is the density of compensating donors with the treated sample having at least a factor of 10^4 lower donor density than in the untreated sample. This reduction in compensation was consistent with the temperature dependent mobility behavior, see Figure II.D.ii.4, which shows a sharp drop in Hall mobility as temperature is decreased for both samples, but with the decrease beginning at a much higher temperature for the uncontaminated sample. This rapid mobility decrease is caused by the onset of hopping conduction, which is related to the number of compensating donors.[14] The reduction in electrical compensation is somewhat surprising given that the expected role of Na is as either an isovalent substitution for Cu or a double acceptor if on an In site. A likely explanation is that Na acts to increase point defect mobility, which allows oppositely charged defects to cluster, rather than passivating donors directly (see discussion below). This idea is consistent with previous work which found that the presence of Na enhanced grain growth and preferred orientation in polycrystalline CIGS layers.[10,11]

Similar results were obtained for two samples treated with Na_2Se. Because the electrical behavior of CIS 150 and CIS 152 were virtually identical, only results for CIS 150 are shown in Figures II.D.ii.5 and II.D.ii.6. One difference between the Na_2Se and NaOH contaminated samples is that samples treated with Na_2Se also showed evidence of a range of low density states near the band edge which modified the carrier concentration and mobility results below 40 K. This may suggest a donor density substantially lower than the $3x10^{12}$ cm^{-3} given as the upper limit in Table II.D.ii.II. The reasons for the differences between the NaOH and Na_2Se treated samples are not known, but it seems likely that they are the result of the presence of excess Se. Again, the primary difference between treated and untreated samples is a dramatic reduction in donor density for samples containing Na. It is interesting to note that while the Na concentrations in CIS 150d and CIS 150c differ by only a factor of ~2 the reduction in the donor density is a factor of >300. There are several possible explanations of this result.

When samples without intentionally added Na were annealed in vacuum at 550 °C there was no significant impact on donor density. This has been tested on several samples which are not included in this study in addition to CIS 135. However, CIS 150b, annealed at 600°C, shows an increase in donor density of a factor of ~10 over the as-deposited sample. This may indicate the loss of Se. It is possible that when CIS 150c was annealed at this temperature both Na and Se diffused into the sample. The resulting increased Se content would explain the larger drop in donor density than resulted from Na alone. Presumably the Se atoms filled Se vacancies. Another possibility is that, if Na acts to reduce donor density by increasing point defect mobility, the Na is acting in conjunction with the higher annealing temperature to increase point defect mobility to allow clustering. If this second explanation is correct, the difference in donor density between CIS 135g and CIS 150d may be due to inconsistencies in our annealing procedure rather than the relatively small difference in Na concentration.

The results found here are consistent with previous data in polycrystalline material where Na contamination increased hole densities.[15-18] In these materials $N_A/N_D \approx 1$. Thus, the drastic reduction in N_D may cause much higher room temperature hole concentrations. However, our data are not consistent with the idea that compensation in the bulk material is reduced by enhanced chemisorption of oxygen.

II.D.ii.c. CONCLUSIONS

The results presented here in the absence of any complications introduced by grain boundary or orientation effects show that Na does, in fact, have an electronic effect in CIGS and that this is primarily to reduce electrical compensation. This is not connected with the presence of oxygen or any other impurity we detected. Some effects of changes in the Se content are also evident in agreement with previous studies on bulk single crystals of CIGS.

APPENDIX III

Cu-Mo Metastable Contacts for $Cu(In_{1-x}Ga_x)Se_2$ Solar Cells

This section summarizes the results of publication P2 listed in Appendix I. In addition to this work, results have been presented on Cu-Mo metastable thin films in papers P6, and P7. This work also resulted in U.S. patent No. 5477088. The results demonstrate a novel method of providing adhesion between thin films of many materials, although the specific application is relevant to $Cu(In_{1-x}Ga_x)Se_2$.

Pure Mo and Cu-Mo contact metallizations were produced by magnetron sputtering. The targets were 30.5 cm x 12.7 cm and were located 7.6 cm from the substrates. Four 25 mm x 25 mm Corning 7059 borosilicate or common soda-lime slide-glass substrates were loaded adjacent to each other in a line opposite the center of the target. The Cu-Mo targets were produced by soldering pieces of Cu foil to a Mo target using In solder as shown in Figure III.1. Two targets were tested with different sizes of Cu strips (to adjust the Cu content in the deposited film). Films were deposited over a wide range of deposition pressures from 0.13 to 1.3 Pa (1-10 mTorr) on both borosilicate and soda lime glasses. A pressure of 0.53 Pa (4 mTorr) produced the best adhesion of CIS to Mo. The substrates were unheated with a resulting deposition temperature of 25-35°C. The deposition time was 20 to 40 minutes with film thicknesses of 1 to 2 μm. The deposition rate was thus ~50 nm/min.

CIS films were deposited from magnetron sputtered Cu and In fluxes and evaporated molecular Se at a rate of ~3 μm/hour. The deposition sequence resulted in an initial heavily Cu-rich layer formed at 350-400°C followed by an In-rich layer at 400-525°C. Typical film compositions for the two layers were 30, 23, and 47 atomic percent (at.%) of Cu, In, and Se, respectively, for the Cu-rich deposition and 23, 26, and 51 at.% net composition for the final bilayers. The Cu-rich and In-rich layers were completely intermixed after deposition was complete. CIS deposition temperatures below refer to the maximum temperature used during the deposition of the In-rich layer. The CIS layers were polycrystalline with equiaxed grain sizes increasing with deposition temperature up to 5 μm in diameter.

Heterojunction solar cells were fabricated by the Institute of Energy Conversion at the University of Delaware (IEC). The device active areas were ~0.08 cm^2. All active devices were tested at IEC under an 87.5 mW cm^{-2} simulated solar spectrum. Selected results were verified under 100mW cm^{-2} irradiance in solar simulator analyses at the National Renewable Energy Laboratory (NREL).

The deposited Cu-Mo films had compositions as measured by EDX of 0, 22, and 30 at. % Cu when the fractional area of Cu on the target surfaces was 0, 33, and 46%, respectively. The surface morphology of the as-deposited films was indistinguishable by SEM from the morphology of pure Mo films deposited at the University of Illinois and at other laboratories.[10] No In contamination of the films was detected by SIMS. Cross sectional fractograph studies indicated identical columnar microstructures in both the Mo and Cu-Mo films. The fracture cross section of CIS on pure Mo showed an exposed Mo region ~5 μm wide around the fracture edge where the CIS had failed to adhere and had flaked away during the fracture. On Cu-Mo samples the CIS fracture face was coincident with the Cu-Mo and glass fracture faces. In the as-deposited condition, the Cu-Mo films exhibited only X-ray reflections associated with a bcc Mo structure, see Figure III.2. However, the lattice parameter of films containing 30 at. % Cu was 1.1% smaller than for pure Mo, see Table III.I. TEM analysis and transmission electron diffraction patterns verified this and showed that the deposited layers were fine grained (~10 nm) metastable solid solutions of Cu in Mo. (Cu is normally almost completely insoluble in Mo at equilibrium.)

Annealing the deposited films at 450°C for 60 min resulted in nearly complete phase separation. Cu precipitates appeared among the Mo grains as identified by both microdiffraction and micro-EDX composition analyses in the transmission electron microscope. Electron micrographs and transmission electron diffraction patterns of typical regions of the as-deposited and annealed samples are shown in Figure III.3. The Mo grain size increased during the phase separation. This was striking since the phase separation occurred at only 25% of the Mo melting point. For pure Mo no grain growth would be expected. X-ray diffraction studies (see Figure III.2 and Table III.I) of the annealed films showed the presence of both fcc Cu and bcc Mo, in

agreement with the TEM analyses. The Mo lattice constant was ~0.2% smaller than the bulk value while the Cu lattice constant was within experimental error of the bulk value. A significant change in preferred orientation of the Mo was also observed by XRD with a strong increase in the Mo (110) reflection and consequent loss of intensity in the (211) reflection.

Tape adhesion tests were carried out for CIS on pure Mo layers deposited on Corning 7059 and soda-lime glass as well as on Cu-Mo layers on soda-lime glass. Virtually complete adhesion failure on the first tape was observed consistently for CIS on pure Mo metallizations on both the Corning 7059 and soda lime substrates. CIS on $Cu_{0.22}Mo_{0.78}$ showed no significant improvement in adhesion compared to films on pure Mo. However, for metallizations with 30 at.% Cu, only minor failures around the edges of the metallized area were found after two tape applications.

To determine the influence of annealing of the contact during CIS deposition, CIS layers were produced on both as-deposited and annealed $Cu_{0.3}Mo_{0.7}$ samples. Tape tests showed generally negligible failures after application of two tapes in both cases. Adhesion failures in completed solar cell device structures were similarly reduced on $Cu_{0.3}Mo_{0.7}$ as compared to on Mo back contacts.

SIMS analyses showed relatively abrupt CIS/Cu-Mo and CIS/Mo interfaces with evidence for some CIS in the back contact at 400°C. The depth of the penetration was approximately the same for both Mo and Cu-Mo at this temperature. At 500°C the penetration depth increased moderately for CIS/Cu-Mo layers. No CIS/Mo interfaces formed at 500°C were examined because of massive adhesion failures. The three CIS constituent elements diffused into the metallization at the same rate suggesting that no preferential reaction with any element occurred and that CIS was forming among pure Mo grains rather than reacting with them.

The compositions of CIS layers deposited on $Cu_{0.3}Mo_{0.7}$ were determined by EDX and were compared to results on pure Mo. There was no detectable change in CIS composition for layers deposited at 400°C. CIS deposited at 450°C for 30 min on $Cu_{0.3}Mo_{0.7}$ showed an increase in Cu atom fraction with respect to CIS on pure Mo (for example, from 22 to 24 at.% Cu), see

Table III.II. A comparable further increase in Cu content was observed when the $Cu_{0.3}Mo_{0.7}$ sample was annealed prior to CIS deposition. Films deposited at 500°C on as-deposited $Cu_{0.3}Mo_{0.7}$ showed greater increases in Cu content relative to those deposited at 450°C. These results are consistent with the SIMS analyses and show that diffusion of Cu out of the back contact begins at ~450°C and that pre-annealing of the Cu-Mo increases the Cu mobility during deposition. Because all of the Cu was not dissolved out of the back contact in the annealed case there must have been two mechanisms limiting dissolution of Cu from the back contact -- kinetically limited phase separation in the metastable alloy and conductance limited diffusion among the Mo grains.

As a further indication of the rate of Cu diffusion from the back contact into a film, 2.2 μm-thick $Cu_{0.3}Mo_{0.7}$ back contact layers were exposed to a flux of only In and Se for 60 min at 450°C. Rough 200-800 nm-thick slightly Cu-rich CIS layers formed on the surfaces as shown in Figure III.4. The composition was determined during cross-sectional fractograph SEM analysis by EDX measurements of the middle of the resultant CIS grains. The photon yield from the back contact should have been negligible in this case. The formation of the CIS consumed ~10% of the Cu in the back contact. Apparently, Cu in the back contact could diffuse readily into the overlying layer but was not dissolved so fast that all the Cu in the back contact was consumed in each deposition. Assuming that the results with the pure In and Se flux are similar to the case of CIS deposition, approximately 10% of the Cu in a 2μm thick stoichiometric CIS layer deposited at 450°C for 40 min would be supplied from the substrate, consistent with both the SIMS and the composition analyses of the deposited layers.

At least a portion of the improved adhesion is probably due to reduced residual stresses in the back contact. When phase separation and Mo grain growth occurred at 450°C, long range atom transport should have relieved any residual stress in the back contact. Thus, when the sample was cooled to room temperature, the only remaining stresses would be due to the differential thermal expansion mismatches among the Cu-Mo, glass, and CIS. The similar adhesion results for soda-lime and borosilicate glasses suggest that the thermal expansion mismatch is not a major

problem for the Cu-Mo back contact. The presence of Cu precipitates in the phase-separated back contacts may also permit thermal expansion stress reduction by plastic deformation of the softer Cu. From the perspective of large scale device production this "automatic" stress relief during annealing or CIS growth should make stress-related adhesion relatively insensitive to the back contact deposition conditions. The resulting wider process window should make large scale solar cell production easier.

The improved adhesion strongly affected the uniformity of performance of solar cells. Figure III.5 shows the relative performances of 12 cells fabricated on each of two 25 mm x 25 mm substrates, one coated with pure Mo and the other with a two-phase Cu-Mo metallization. The final compositions were similar. To reduce questions of reproducibility the performances are for the best devices obtained to date on each metallization. The significant improvement in uniformity of the device performances on the Cu-Mo substrate is not due to a change in compositional uniformity, which was ±2 at. % for Cu and In across the substrate in both cases. The improved performance uniformity apparently resulted from a reduction in adhesion failures. Optimal performance in a 0.0745 cm^2 active area device was obtained for a $CuInSe_2$ film deposited on a $Cu_{0.3}Mo_{0.7}$ coated borosilicate glass substrate. The active area performance was: 10.0% conversion efficiency with V_{oc}=426 mV, J_{sc}=35.3 mA cm^{-2}, and a fill factor of 66.5% as measured in the NREL solar simulator under air-mass-one conditions.

Conclusions

The results presented above show that initially metastable solid solutions of Cu in Mo containing approximately 30 at.% Cu can provide significantly increased adhesion to CIS films with consequent improvements in the uniformity of performance of photovoltaic devices. Annealed layers in which phase separation of the Cu from the Mo has occurred show more dissolution of Cu from the back contact than in the unannealed case but yield similar increases in adhesion. The metastable solution appears to provide a rate limited supply of Cu to the back of the CIS layer that should result in a Cu-rich layer at least over some small distance from the contact

even though the Cu composition is relatively constant throughout the remainder of the layer. Under typical device production conditions used in this work, approximately 10% of the Cu in the CIS layer is supplied from the back contact. This is sufficient to provide a strong chemical and mechanical bond to the substrate but not so much as to significantly alter the back contact properties.

APPENDIX IV

Electroluminescence from $Cu(In_{1-x}Ga_x)Se_2$ Solar Cells

This section summarizes the results of publication C4 listed in Appendix I. Further analyses of these devices is ongoing. One of the critical problems facing the $CuInSe_2$ solar cell community is a lack of fundamental understanding of the operation of $CuInSe_2$ solar cell devices. A critical missing piece of information required for more accurate modeling is an understanding of the mechanisms by which minority carriers recombine in the solar cell. One of the possible pathways for such recombination is by radiative processes. These can be characterized directly by observation of the emitted light as a function of device operation conditions. The remaining recombination occurs by non-radiative processes. Thus, a study of radiative recombination provides information on non-radiative events as well. It is thus of interest to examine light emission from high efficiency polycrystalline $Cu(In,Ga)Se_2$ solar cells.

The solar cells studied in this work were obtained from three groups in different laboratories. In each case, a number of devices were available for test on each sample. The results reported are typical of measurements on several of the devices in each set. The $CuInSe_2$ solar cell group at the National Renewable Energy Laboratory (NREL) supplied devices with performances exceeding 14% efficiency. The absorber layers for these devices were produced by thermal evaporation and had graded Ga contents with Ga/(In+Ga) ratios ranging from ~0.20 at the front face to ~0.50 at the back contact. Devices supplied by Siemens Solar Industries (SSI) were above 13% efficient, and contained essentially no Ga. Two sets of devices produced by thermal evaporation were supplied by the Institute for Energy Conversion at the University of Delaware (IEC). The first set had a uniform Ga/(In+Ga) ratio of 0.36 with >12% efficiency. A second set had a Ga ratio of 0.57 and >11% efficiency.

The devices were mounted on an optical bench when tested at room temperature or in a vacuum cryostat when tested as a function of temperature. Forward bias voltages were provided by a Hewlett Packard pulse generator or, at low powers, by a dc current supply. Current-voltage curves were obtained from these measurements. Shunt and series resistances were obtained using

standard diode equations. Emitted light was focused through a pair of lenses onto a 2 mm x 4 mm PbS photodetector cooled to 190 K. A mechanical chopper was located between the solar cell and the photodetector and the luminescence signal was detected with a lock-in amplifier. Measurements of the wavelength dependence of the emitted light were made by inserting a Kratos monochromator between the solar cell and the chopper. The monochromator used a near infrared grating having 590 grooves/mm. For the higher light intensities a neutral density filter was used to insure a linear response of the PbS detector. The transmission and resolution of the monochromator could also be adjusted by opening and closing its entrance and exit slits. The monochromator resolution was verified for different slit widths using a Xe arc lamp light source. With the widest entrance and exit slits used, the monochromator wavelength resolution was 10 nm. The response of the PbS detector was calibrated as a function of wavelength by replacing the solar cell in the spectral response configuration with a calibrated optical pyrometer. The Xe lamp emission spectrum was known and hence the total light flux could be determined for a given wavelength selected in the monochromator.

The spectral response of the solar cells was measured with the same instruments by replacing the solar cell with the Xe lamp. A beam splitter was placed after the monochromator. The solar cell was situated in one of the split beams and the PbS detector in the other. The PbS detector was used to calibrate the relative light intensity striking the solar cell. The solar cell short circuit current density was then recorded while varying the wavelength of the incident light. As a final check, both red (750 nm) and infrared (1300 nm) commercial light emitting diodes (LED's) were characterized and the emitted intensities as a function of bias current were measured and compared with the diode specifications.

For temperature-dependent studies the solar cells were mounted on the cold tip of a recirculating He refrigerator using spring-loaded pins. These also served to make electrical contact to the device. The temperature was monitored using a Pt resistance-temperature detector attached to the cold tip next to the sample.

Electroluminescence was detected for all devices tested. The luminescence intensity increased with increasing bias current, after correcting for shunt resistance, according to a power law: $L = aJ^n$ where L is the luminescence intensity, J is the current density, and a and n are constants. The exponent of the current, n, ranged from ~1.2 to ~1.9 and was larger for the more efficient solar cells. However, no specific relationship was found between cell parameters and n. The efficiency of the luminescence increased with increasing current density in all devices at room temperature. The value of a varied from device to device.

Based on calibrations of the detection apparatus, the quantum efficiency of the devices was determined as a function of current density. The results for the NREL device are shown in Figure IV.1 along with values for a commercial infrared LED. Note that the drive current has not been corrected for shunt resistance. The decrease in efficiency of the NREL device at low temperature and high drive currents probably results from heating of the cell.

The commercial device has an active area of 3.24×10^{-4} cm^2, approximately 1000 times smaller than the solar cell. Thus, the current density is larger by a corresponding factor. Furthermore, the IR LED is optimized for efficient focusing of emitted light into a small angle whereas the solar cell light emission will be reduced by internal reflections, absorption, and scattering. Hence, the effective internal quantum efficiency of the solar cell was estimated to be a factor of ~250 times larger than the observed external value. This suggests that the internal quantum efficiency of the solar cell may be comparable to that of the commercial LED.

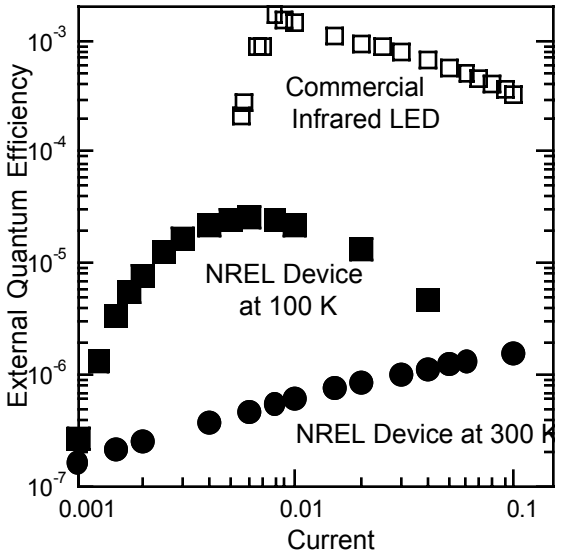

Figure IV.1. External quantum efficiency for the NREL solar cell tested at 300 K (black circles) and 100 K (black squares) and a commercial IR light emitting diode (open squares). Measurements were made without the monochromator in place.

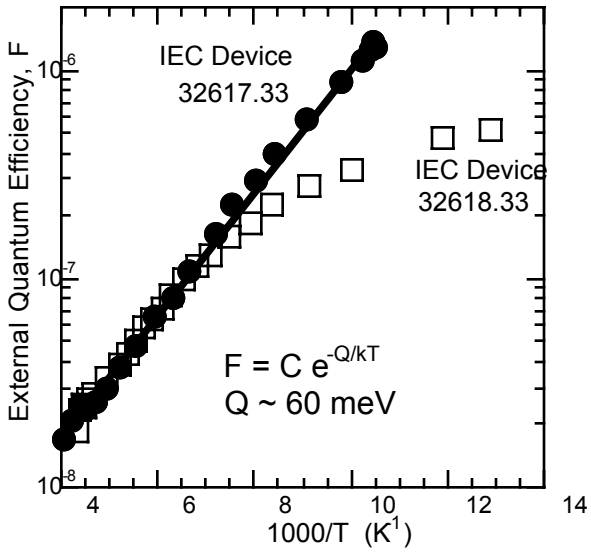

Figure IV.2. Shows the external quantum efficiency for the IEC devices as a function of temperature (in Kelvin) measured at 0.01 A/cm² forward current density.

Figure IV.2 shows the details of the effect of temperature on external quantum efficiency of the IEC devices. The efficiency increases exponentially with decreasing temperature with a characteristic slope of 60 meV. The device with the higher Ga content ([Ga/In+Ga]=0.57) shows saturation at low temperature while the device containing less Ga (III ratio of 0.36) shows no saturation. The data suggest that decreasing the temperature is continuously freezing out some non-radiative recombination process.

The electroluminescence spectrum and spectral response for the NREL solar cell is shown in Figure IV.3. Curves for the other solar cells tested look similar. The peak luminescence energy was constant as a function of junction current, indicating that saturation of states through which radiative recombination was taking place did not occur.

All luminescence spectra were fit with Gaussian functions. The luminescence spectra consisted of one or two approximately Gaussian peaks as shown in Figure IV.3. The SSI and IEC device 32617.33 did not clearly show the weak peak but had relatively broad symmetric tails in their spectra. Detection of the weak peaks in the NREL and IEC 32618.33 devices was significantly facilitated by low temperature measurements that emphasize this peak. The relative intensities and positions of the fit peaks changed upon cooling of the devices. In general, the weaker peak remained unchanged in both position and full width at half maximum (FWHM) but increased significantly in intensity. The main peak shifted to longer wavelength (lower energy), decreased in breadth, and changed in amplitude. The results of the peak fits are shown in Table IV.I.

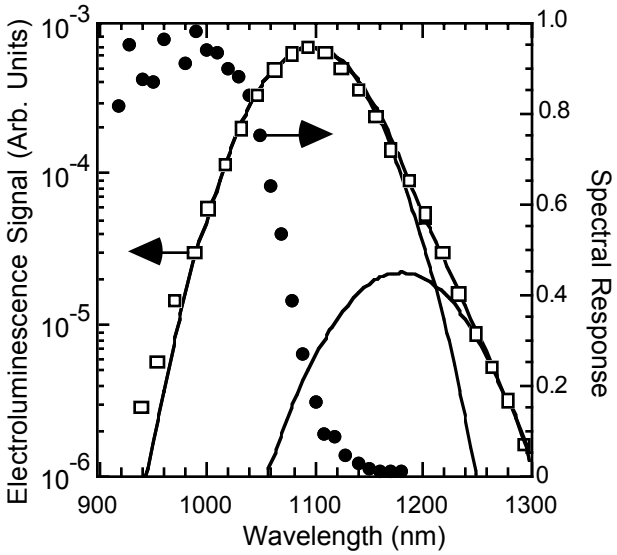

Figure IV.3: Spectral response and electroluminescence data for the NREL device tested. Also shown are the Gaussian curves fit to the electroluminescence data. The electroluminescence data was recorded at a current density of 0.1 A/cm^2.

None of the devices showed luminescence spectral widths that were significantly affected by the spectral response of the monochromator or detector, thus the entrance and exit slits of the monochromator were typically operated fully open. In addition, the peak widths are much wider than can be explained by thermal fluctuations. This suggests that the peak width may be due to variations in the energies of the states participating in radiative recombination.

Cooling of two of the devices resulted in shifts in the peak position of the luminescence to longer wavelengths (lower energies) which was not the result of changes in intensity of the two Gaussian components of the peak (see Figure IV.4). This shift to longer wavelengths is surprising as the energy gap is expected to increase as the temperature decreases. For comparison, the low-temperature spectral response was measured and is also shown in Figure IV.4. Clearly the carrier generation shifts to higher energies as the temperature decreases, as expected.

Table I

Primary Peak, 300 K

Device Designation	Peak λ (nm)	FWHM (nm)	Peak Area arb units	Ga /(In+Ga)
IEC 32617.33	1090	158	7.1	0.36
IEC 32618.33	1050	166	5.9	0.57
NREL S578B14	1097	100	360	graded
SSI	1243	126	400	0.00
IR LED	1281	117	--	--

Secondary Peak, 300 K

IEC 32618.33	1225	117	0.5	0.57
NREL S578B14	1180	117	137	graded

Primary Peak, 70 K

IEC 32618.33	1097	140	47	0.57
NREL S578B14	1110	82	210	graded

Secondary Peak, 70 K

IEC 32618.33	1225	117	8.7	0.57
NREL S578B14	1180	117	106	graded

The Siemens Solar (SSI) and IEC 32617.33 devices have not yet been tested at 70K.

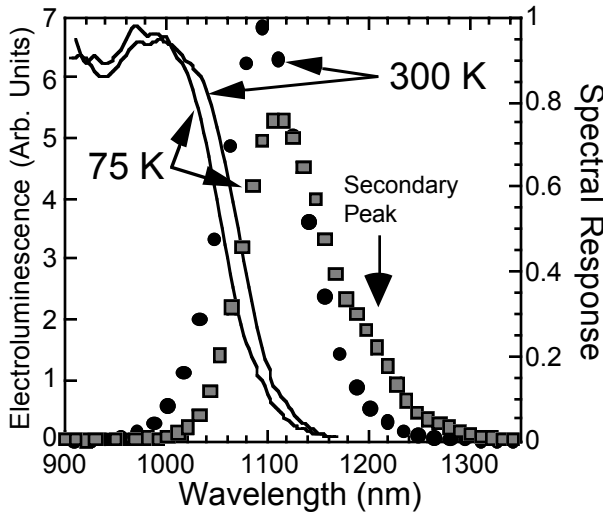

Figure IV.4. Comparison of the electroluminescence and spectral response from the NREL solar cell. The electroluminescence was obtained at 0.1 A/cm^2 current.

The peak in the electroluminescence and the onset of spectral response increase with Ga content, consistent with the increasing energy gap of the material. Although the data is too noisy to draw definite conclusions, it appears that the luminescence peak shifts in roughly the same manner as the onset of photovoltaic response. This will be investigated shortly using a series of devices selected to provide changes of Ga content in otherwise similar devices.

CONCLUSIONS

The electroluminescence observed from forward biased solar cells suggests that at low temperatures a significant fraction of the carriers recombine radiatively. The width of the spectral response is large indicating a range of states contributing to radiative recombination. In some devices, subsets of these states can be resolved as distinct populations with different temperature dependencies. The effect of temperature is also different for the radiative recombination process and the carrier generation process responsible for spectral response. This implies that radiative recombination occurs between states near the band edge but does not follow the usual temperature dependence observed for the band edge.

REFERENCES

1. P. Blood and J. W. Orton, *The Electrical Characterization of Semiconductors: Majority Carriers and Electron States, Techniques of Physics: 14* (Academic Press, New York, 1992).

2. see for example C. M. Wolfe, N. Holonyak, Jr., and G. E. Stillman, Physical Properties of Semiconductors, Prentice-Hall, 1989.

3. A. Rockett and R. W. Birkmire, *J. Appl. Phys.,* **70** (7) 81-97, 1991.

4. S. M. Wasim, *Solar Cells*, **16**, 1986, p. 289.

5. J. D. Wiley, *Semiconductors and Semimetals, volume 10 (Transport Phenomena)*, (Academic Press, New York, 1975).

6. C. Erginsoy, *Phys. Rev*., **79**, 1950, p. 1013.

7. N. Mott, *Metal-Insulator Transitions*, (Barnes & Noble Books, New York, 1974).

8. J.-Y. Hou, private communication.

9. M. Marudachalam, H. Hichri, R. W. Birkmire, J. M. Schultz,A. B. Swartzlander, and M. M. Al-Jassim, *Proceedings of the 24st IEEE Photovoltaic Specialists Conference, 1996* (IEEE, New York, 1996).

10. M. Bodegård, L. Stolt, and J. Hedström, *Proceedings of the 12th European Photovoltaic Solar Energy Conference,* 1994 Ampsterdam, p. 1743.

11. V. Probst, J. Rimmasch, W. Riedl, W. Stetter, J. Holz, H. Harms, and F. Karg, *Proceedings of the 1st World Conference on Photovoltaic Energy Conversion, 1994* (IEEE, New York, 1994), p. 144.

12. J. Holz, F. Karg, and H. von Philipsborn, *Proceedings of the 12th European Photovoltaic Solar Energy Conference,* 1994 Ampsterdam, p.1592.

13. M. Ruckh, D. Schmid, M. Kaiser, R. Schäffler, T. Walter, and H. W. Schock, *Proceedings of the 1st World Conference on Photovoltaic Energy Conversion, 1994* (IEEE, New York, 1994), p. 156.

14. U. Rau, M. Schmitt, D. Hilburger, F. Engelhardt, O. Seifert, and J. Parisi, *Proceedings of the 25th IEEE Photovoltaic Specialists Conference, 1996* (IEEE, New York, 1996), p. 1005.

15. H. Neumann, E. Nowak, B. Schumann, and G. Kühn, Thin Solid Films, **74**, p. 197, 1980.

16. B. Schumann, A. Temple, G. Kühn, H. Neumann, N. Van Nam, and T. Hänsel, Kristall und Technik, **13**(11), p. 1285, 1978.

17. B. Schumann, A. Temple, G. Kühn, H. Neumann, N. Van Nam, and T. Hänsel, Thin Solid Films, **52**, p. 45, 1978.

18. B. Schumann, H. Neumann, A. Temple, G. Kühn, and E. Nowak, Kristall und Technik, **15**(1), p. 71, 1980.

TABLES:

Table II.A.I. The correlations between the extra reflections and the defects in the $CuIn_3Se_5$ phase.

Extra Reflections	Associated Defects
(001), (010), (001), (002), (110), (012), (102), (1 $\bar{2}$ 2), ($\bar{2}$ 12)	Ordered Point Defects
Streaks along {112} reflections, ($\bar{2}$ $\bar{2}$ 8)/3, ($\bar{2}$ 4 $\bar{4}$)/3, (4 $\bar{2}$ $\bar{4}$)/3, ($\bar{4}$ $\bar{4}$)/3, (24 $\bar{4}$)/3, (2 $\bar{2}$ 8)/3, ($\bar{4}$ $\bar{2}$ 4)/3, (224)/3, (2 $\bar{2}$ $\bar{8}$)/3, ($\bar{2}$ 44)/3, ($\bar{2}$ $\bar{2}$ $\bar{8}$)/3, (4 $\bar{2}$ 4)/3	Planar Defects (Stacking Faults and Nanotwins)
{103}, {101}	Three Dimensional Domains

Table II.C.I: Composition and Diffusivity of Ga

Sample	Cu/In	I/III	D [cm^2/s]
CIS 69	0.43	0.33	$7x10^{-12}$
CIS 133	0.68	0.55	$3.5x10^{-12}$
CIS 67	0.89	0.63	$7.1x10^{-13}$
CIS 134	0.90	0.74	$4.2x10^{-13}$
CIS138	0.94	0.76	$2.7x10^{-13}$
CIS 61	0.96	0.74	$4.2x10^{-13}$
CIS 137	0.99	0.72	$3.3x10^{-13}$
CIS T2	1.00	0.79	$5.5x10^{-13}$
CIS 24	1.19	0.75	$3x10^{-11}$
CIS 25	1.41	0.71	$5x10^{-11}$

Table II.D.ii.I: Annealing conditions and sodium contamination levels.

Sample	anneal conditions	Na source	Na level (SIMS) [cm^{-3}]
CIS 135a	none	none	$6.2x10^{17}$
CIS 135f	5 min 550 °C	none	$6.2x10^{17}$
CIS 135g	5 min 550 °C	NaOH	$6.0x10^{19}$
CIS 150a	none	none	$9.0x10^{17}$
CIS 150b	10 min 600 °C	none	$4.5x10^{17}$
CIS 150c	10 min 600 °C	Na_2Se	$1.1x10^{20}$
CIS 150d	10 min 550 °C	Na_2Se	$5.8x10^{19}$
CIS 152a	none	none	$4.7x10^{17}$
CIS 152b	10 min 600 °C	none	$4.3x10^{17}$
CIS 152c	10 min 600 °C	Na_2Se	$1.1x10^{20}$

Table II.D.ii.II: Fitting parameter values for carrier concentration vs. temperature data.

Sample	deep acceptor density [cm^{-3}]	deep acceptor activation energy [eV]	shallow acceptor density [cm^{-3}]	shallow acceptor activation energy [eV]	compensating donor density [cm^{-3}]
CIS 135a	$3.00x10^{18}$	0.172	$7.70x10^{15}$	0.040	$7.30x10^{15}$
CIS 135f	$1.10x10^{18}$	0.155	$7.40x10^{15}$	0.038	$6.60x10^{15}$
CIS 135g	$1.03x10^{18}$	0.142	$7.50x10^{15}$	0.038	$<7x10^{11}$
CIS 150a	$2.20x10^{18}$	0.175	$7.35x10^{15}$	0.034	$7.40x10^{15}$
CIS 150b	$5.80x10^{17}$	0.110	$7.35x10^{15}$	0.034	$6.0x10^{16}$
CIS 150c	$1.85x10^{18}$	0.162	$7.35x10^{15}$	0.034	$<3x10^{12}$
CIS 150d	$2.10x10^{18}$	0.162	$5.70x10^{15}$	0.034	$1x10^{15}$
CIS 152a	$1.50x10^{18}$	0.168	$7.35x10^{15}$	0.034	$7.40x10^{15}$
CIS 152b	$1.20x10^{18}$	0.155	$1.40x10^{16}$	0.034	$1.8x10^{15}$
CIS 152c	$1.40x10^{18}$	0.162	$7.35x10^{15}$	0.034	$<3x10^{12}$

Table III.I. X-Ray Diffraction Results For Cu_xMo_{1-x} Films

	Interplanar Spacing in Å (Intensity in counts/sec)			
Metallization	Mo (110)	Mo (211)	Cu(111)	Cu (200)
Mo as deposited	2.225 (24,000)	1.281 (161)		
$Cu_{0.22}Mo_{0.78}$	2.220 (5159)	1.278 (12,794)		
$Cu_{0.3}Mo_{0.7}$ as deposited	2.200 (247)	1.271 (656)		
$Cu_{0.3}Mo_{0.7}$ annealed	2.221 (4014)	1.281 (151)	2.089 (2205)	1.805 (192)

FIGURES

Figure II.A.1. (a) The absorption coefficient, α, plotted as $(\alpha E)^2$ as a function of photon energy, E, and (b) a typical cathodoluminescence spectrum for the epitaxial ordered vacancy compound layer.

Figure II.A.2. (a) A dark-field TEM micrograph formed by using the (200) superlattice reflection showing antiphase domain boundaries. (b) A g(3g) weak beam dark-field TEM image showing dislocations (some indicated by arrow heads), stacking faults, and nanotwins.

Figure II.A.3. High resolution TEM micrographs taken along $[1\,\bar{1}\,0]$ of (a) stacking faults (arrow heads mark fault planes) and (b) a nanotwin labeled "T". Both the stacking faults and the nanotwin exhibited (112) habit planes.

Figure II.A.4. A bright field plan view TEM micrograph from a rapid-thermal-annealed sample showing the dislocation structure.

Figure II.A.5. Experimental (a) and calculated (b) and (c) [001] zone-axis diffraction patterns. Simulations included (b) ordered In-on-Cu site point defects or (c) domains with unit cells rotated by 90° around (100) or (010).

Figure II.A.6. Experimental (a) and computer simulated (b) [021] zone-axis diffraction patterns. (100)- and $(01\,\bar{2})$-type spots resulted from the ordering of the point defects, and streaks along $(1\,\bar{1}\,2)$ and (11) diffraction vectors from stacking faults and nanotwins.

Figure II.A.7. Experimental (a) and a computer simulated (b) [221] zone-axis diffraction patterns. Extra reflections marked by arrow heads in (a) are produced by stacking faults and nanotwins. Other extra reflections result from the ordered defect structure.

Figure II.A.8. (a) A high-resolution plan-view electron micrograph taken along [001]. Two domains marked by D1 and D2, respectively have unit cells rotated with respect to eachother. The domain boundary is indicated by arrow heads. The corresponding experimental (b) and simulated (c) diffraction patterns are also shown.

Figure II.A.9. [021] (a) and [221] (b) selected area diffraction patterns from a sample which had been heat treated at 700°C for 60 sec in a rapid thermal annealing system.

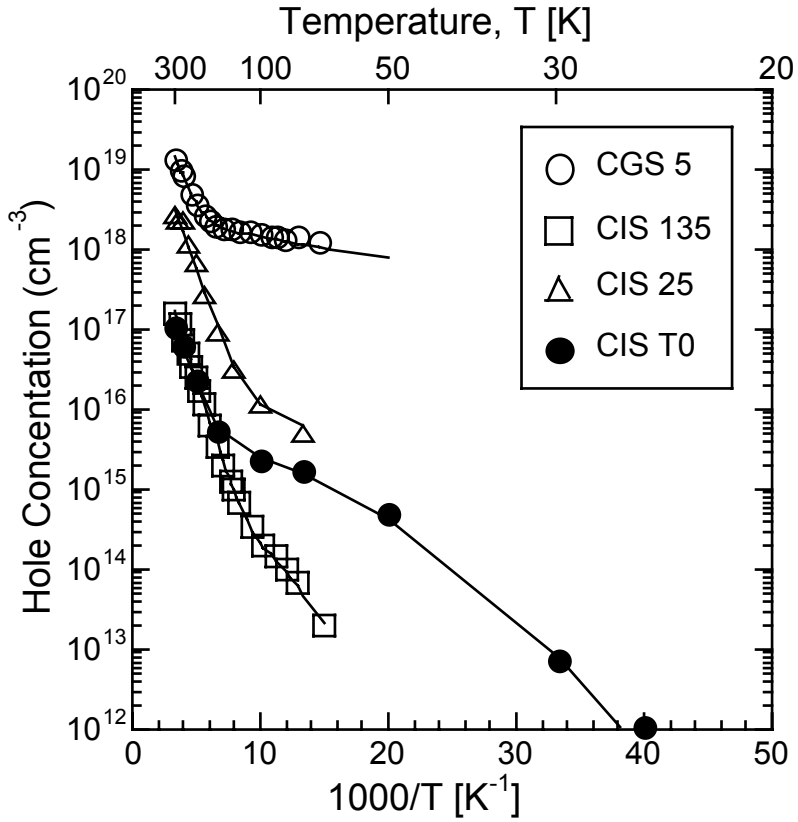

(Figure II.B.1a above)

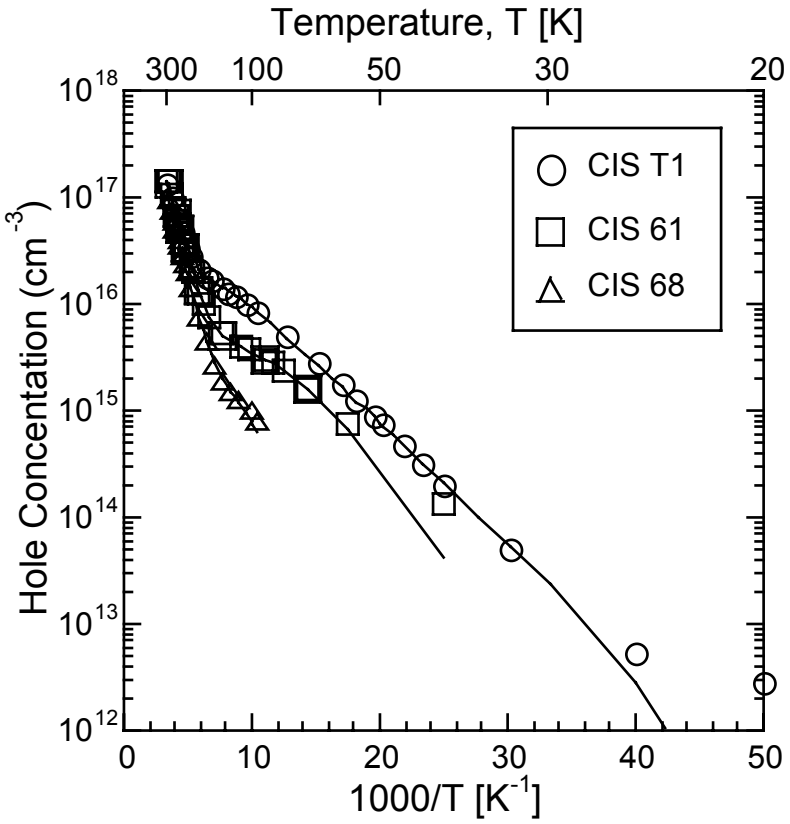

(Figure II.B.1b above)

Figure II.B.1.: Experimental and calculated hole concentrations as a function of inverse temperature for several samples. a) Values for four samples for which the Ga concentration was approximately constant. b) Values for three samples for which the Ga concentration followed a roughly error-function decrease from the back surface to the front surface of the sample. Note that the calculated concentrations fall below the measured concentrations at low temperature due to hopping conduction in films with very low compensation levels.

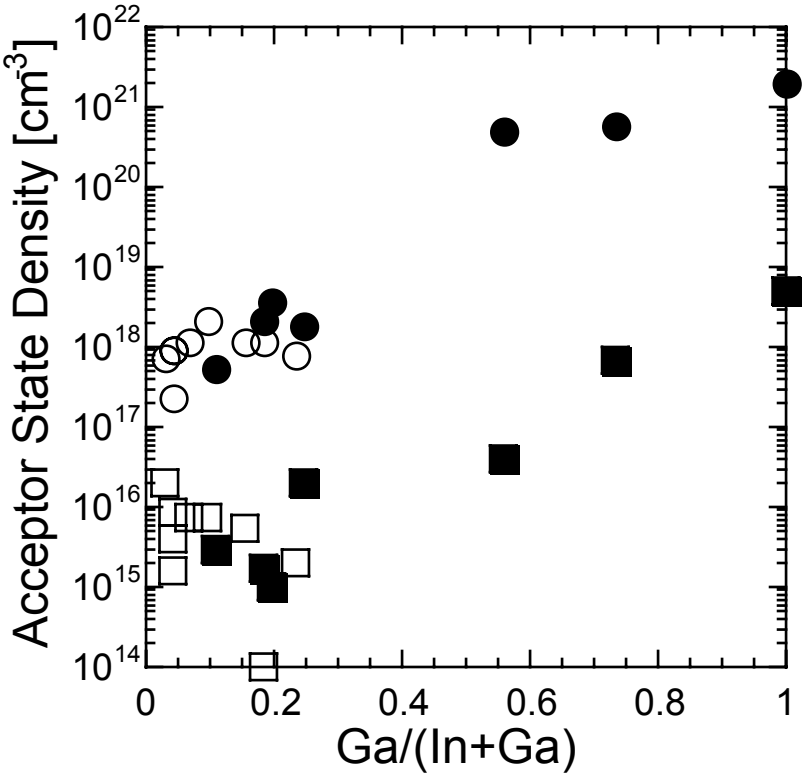

Figure II.B.2: Values of acceptor density as a function of Ga content. Circles indicate values for N_{a1} and squares indicate values for N_{a2}. Open points indicate samples containing a significant Ga gradient while the Ga concentration is relatively uniform in samples for which solid points are plotted.

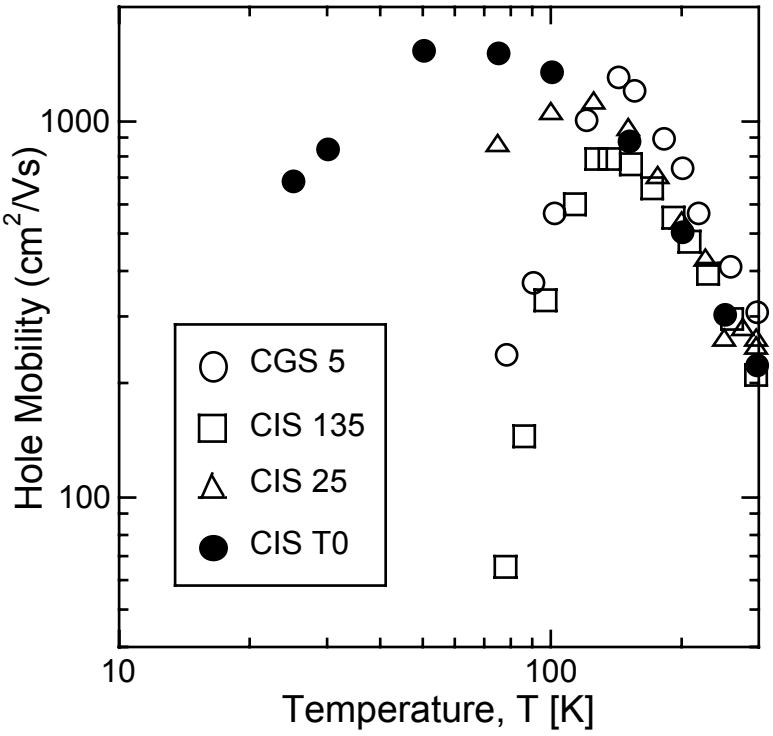
Hole Mobility (cm²/Vs)
1000
100
10
100
Temperature, T [K]
CGS 5
CIS 135
CIS 25
CIS T0

(a) above

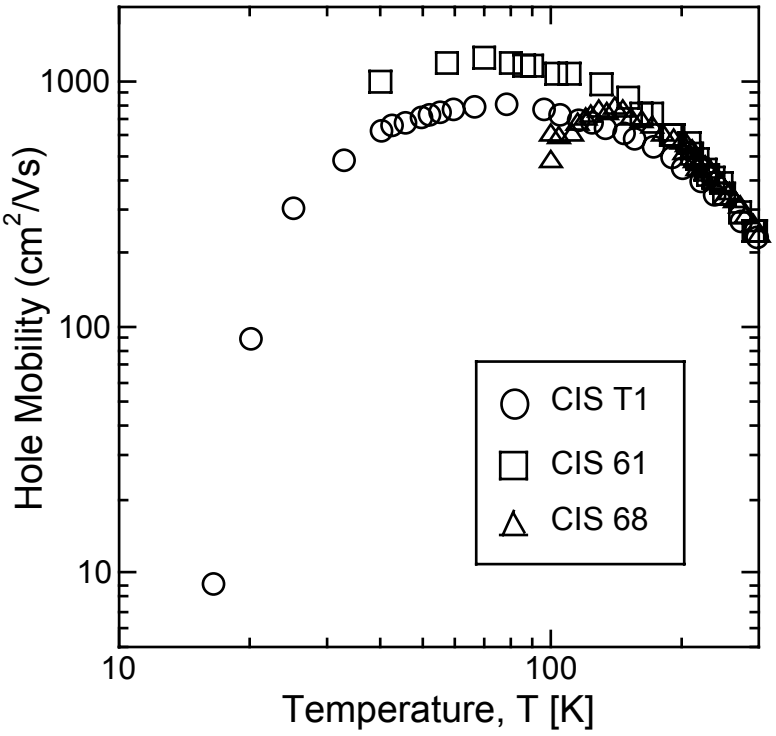

(b) Above

Figure II.B.3: Hall mobility vs. temperature for the samples shown in Figures II.B.1a and II.B.1b, respectively.

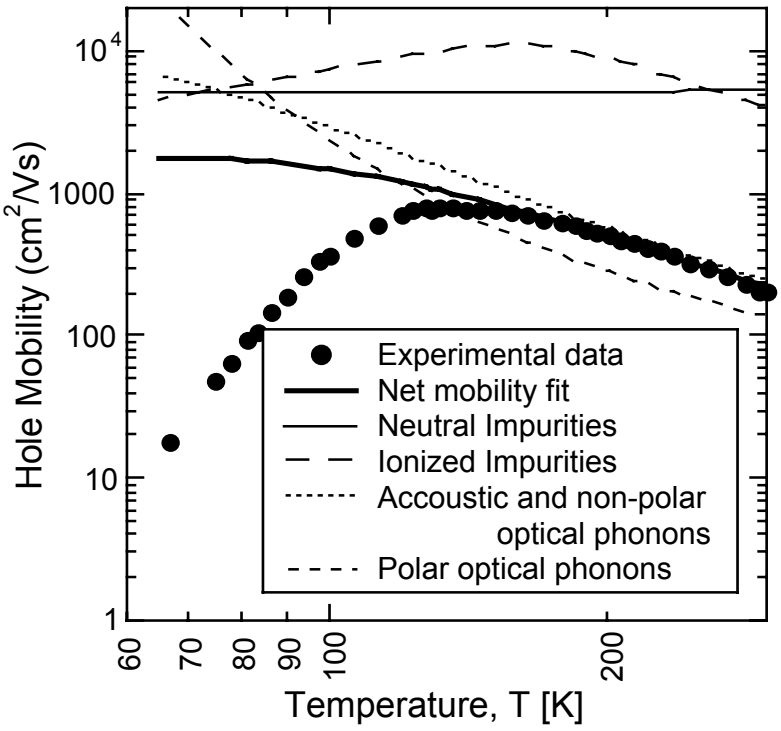

Figure II.B.4: Experimental and calculated mobility vs. temperature for CIS 135 showing contributions from neutral impurities, ionized impurities, acoustic and non-polar optical phonons, and polar optical phonons.

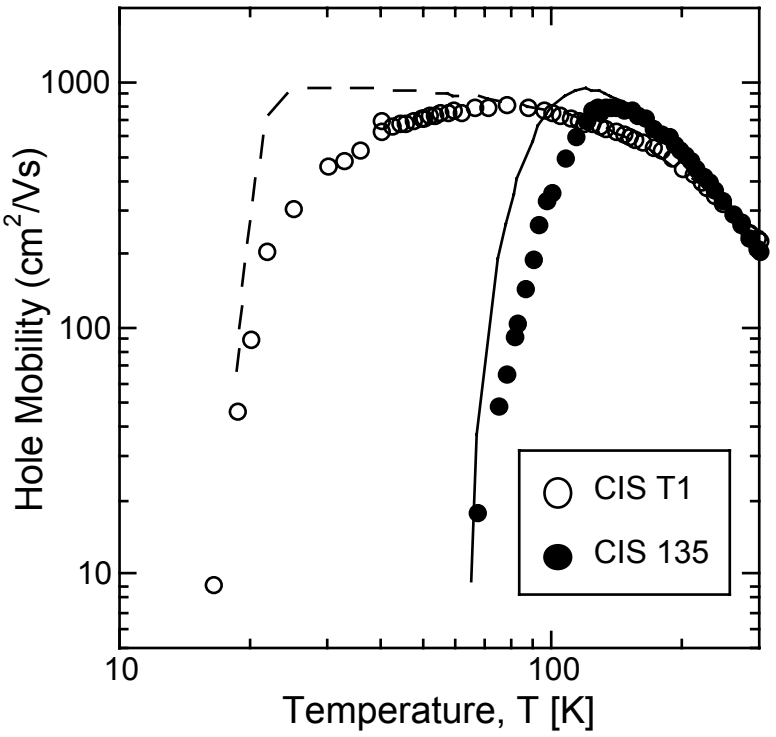

Figure II.B.5 Experimental (points) and calculated (lines) apparent mobility for CIS T1 and CIS 135 including contributions from hopping conduction.

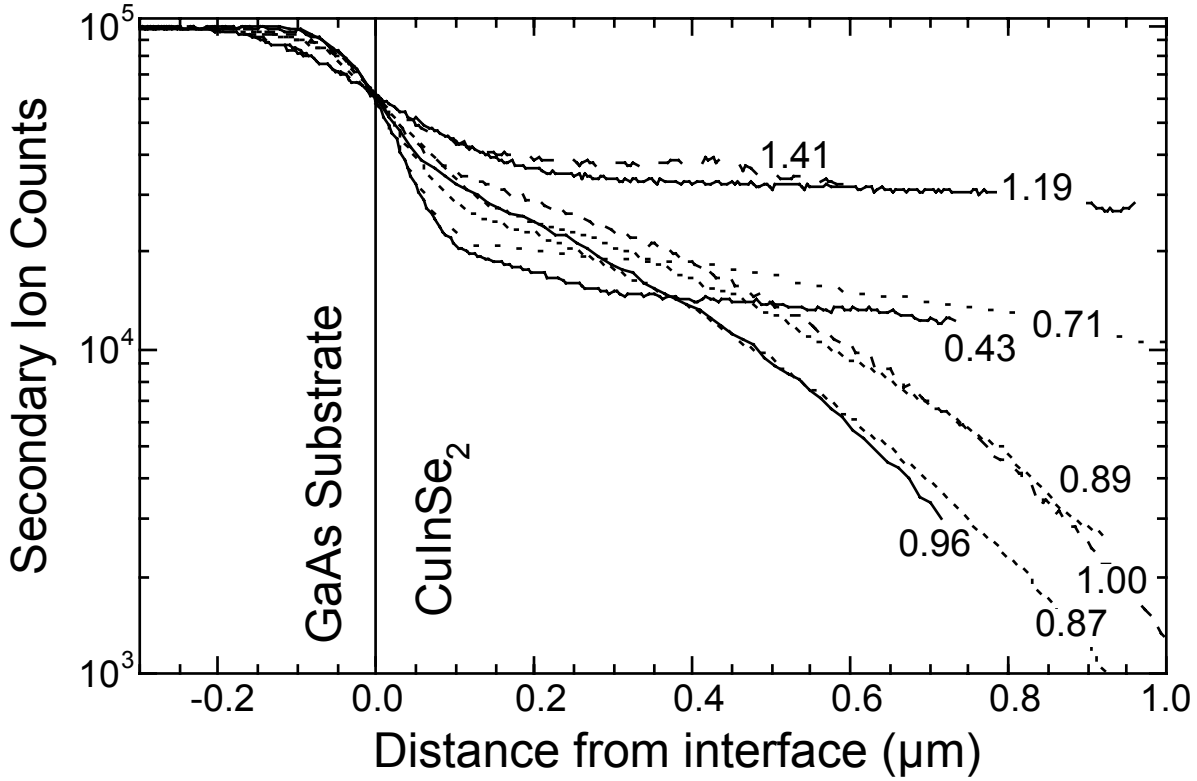

Figure II.C.1: Measured Ga count rate vs. distance from the CIS/GaAs interface for various Cu/In ratios (ratios are listed with each curve). Count rates were approximately equal but have been adjusted to 1.0×10^5 counts. The x-axis was defined with x=0 at the point where the Ga signal had dropped by 40% from its value in the GaAs.

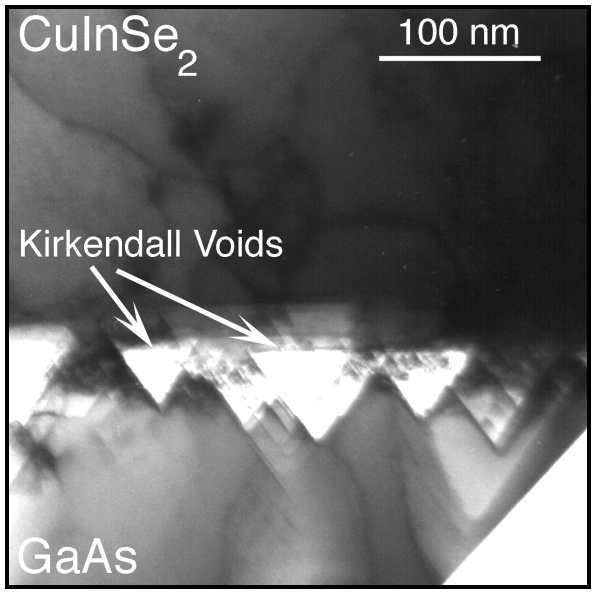

Figure II.C.2: A cross-sectional transmission electron micrograph of the GaAs/$CuInSe_2$ interface showing the presence of Kirkendall voids in the GaAs.

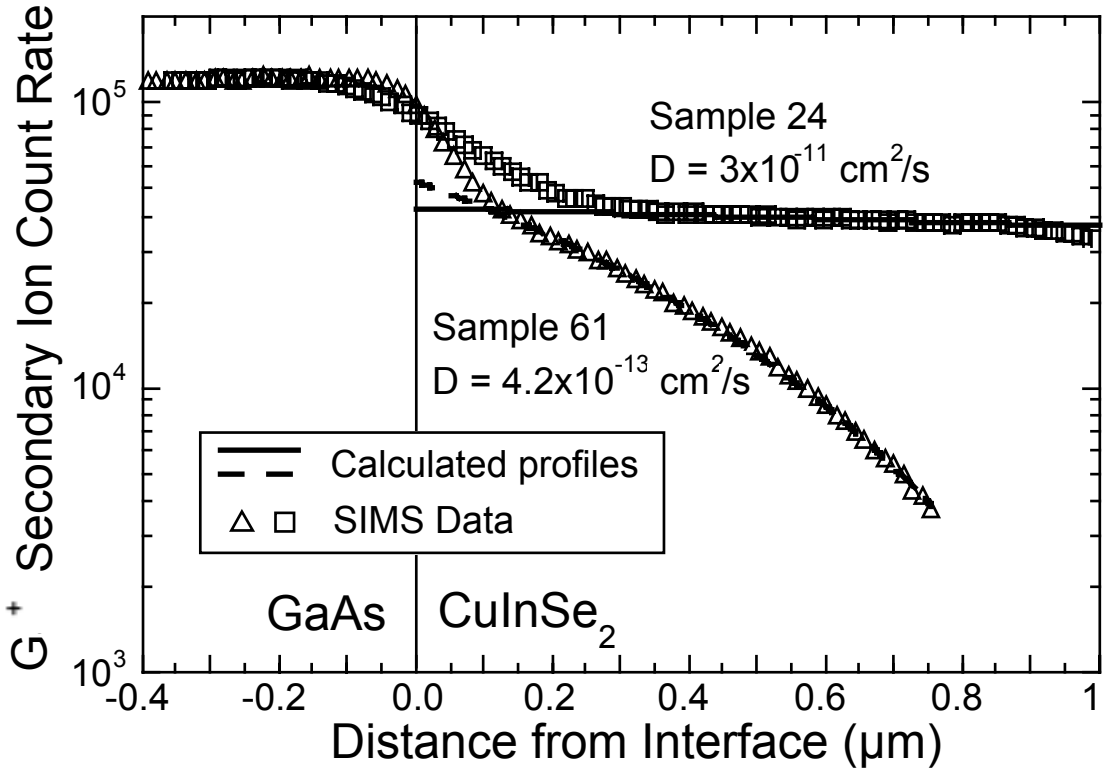

Figure II.C.3: Fits to experimentally determined Ga profiles in samples with Cu/In=0.96 and 1.19.

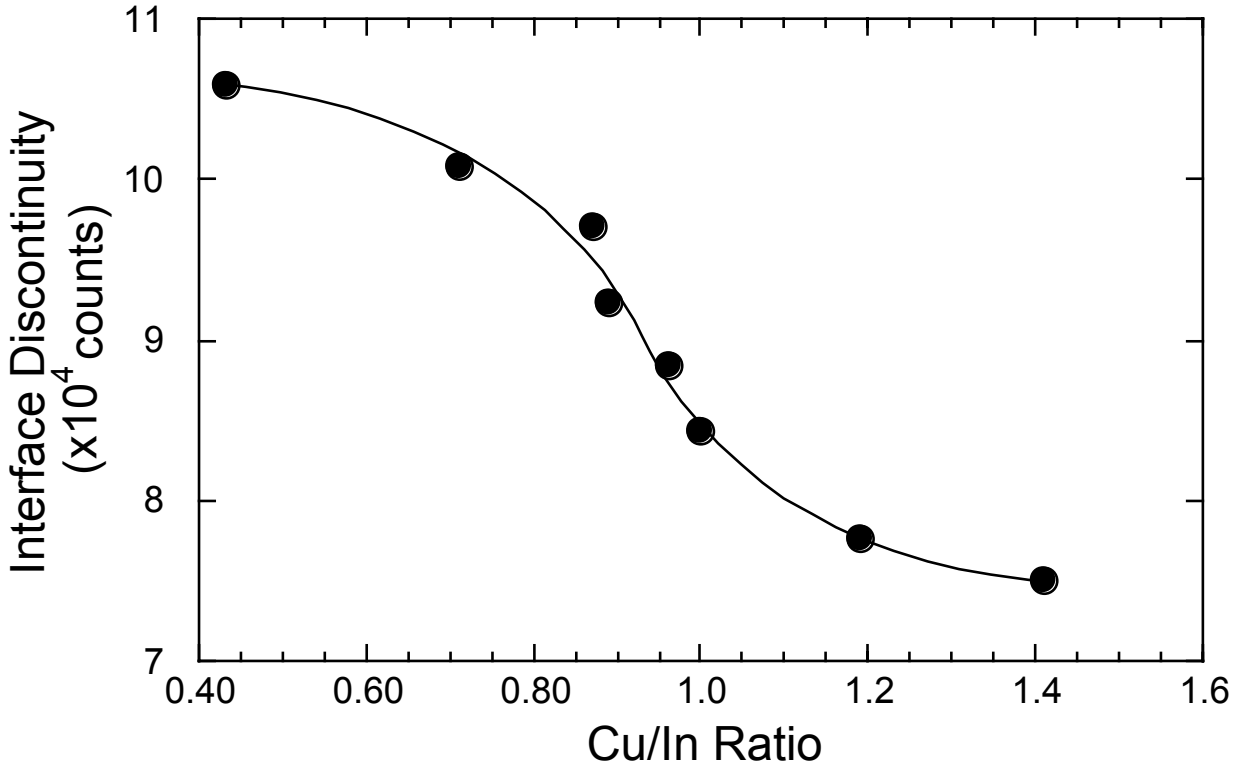

Figure II.C.4: The discontinuity in Ga^+ count rate at the $CuInSe_2$/GaAs interface.

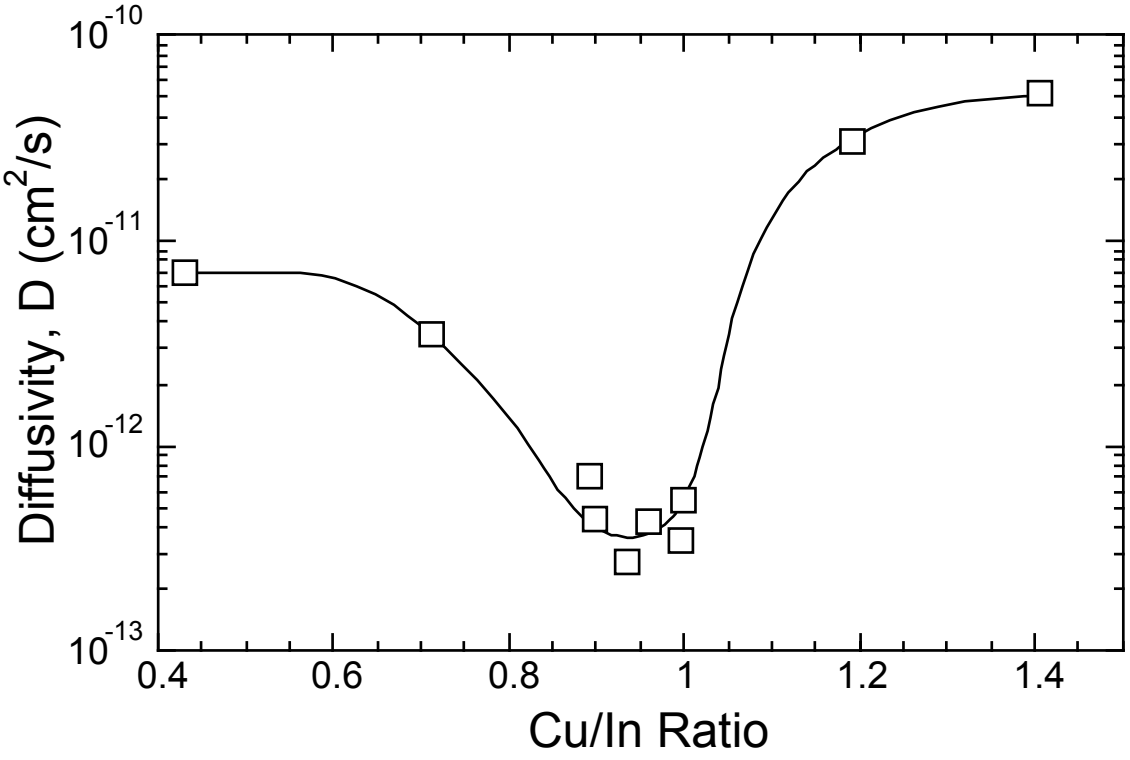

Figure II.C.5: Diffusivity of Ga is $CuInSe_2$ vs. Cu/In ratio at 725°C. The curve drawn through the data is an estimate of the most likely behavior which fits the data.

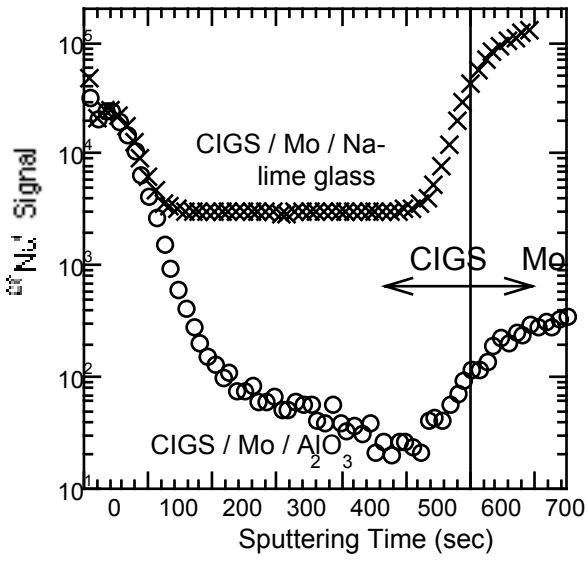

Figure II.D.i.1. SIMS profiles of the Na concentration in CIGS films deposited on sputtered Mo on two substrates: Na-lime glass (X's) and Na-free Al_2O_3 (open circles).

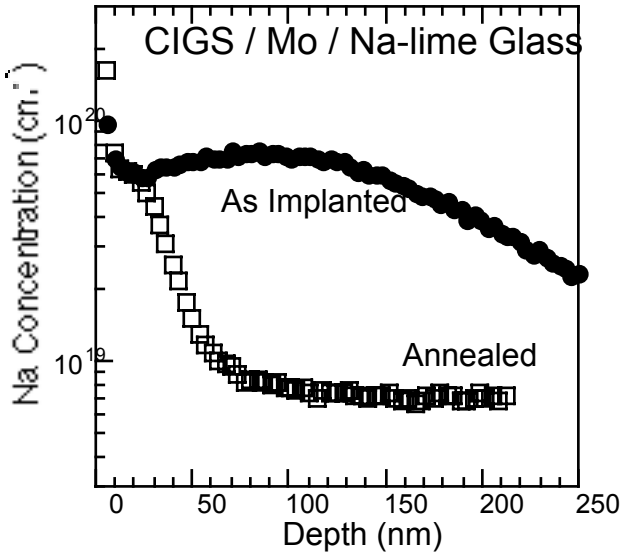

Figure II.D.i.2. SIMS profiles of the Na concentration in a CIGS layer on Mo on Na-lime glass (also shown in Fig. II.D.i.1) as implanted (solid circles) and after annealing (open rectangles). The Na signal was converted to a concentration based on the simulated implant and the annealed sample conversion was accomplished by matching the Cu signal levels (not shown) for the two profiles.

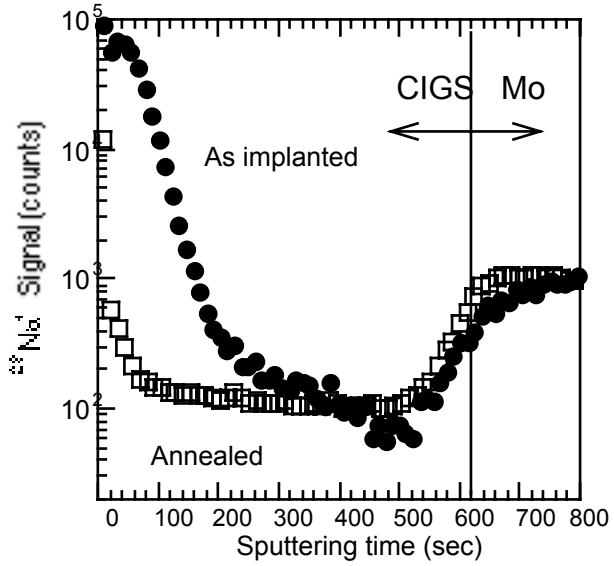

Figure II.D.i.3. As implanted (filled circles) and annealed (open squares) Na profiles for the CIGS sample on Mo on Al_2O_3.

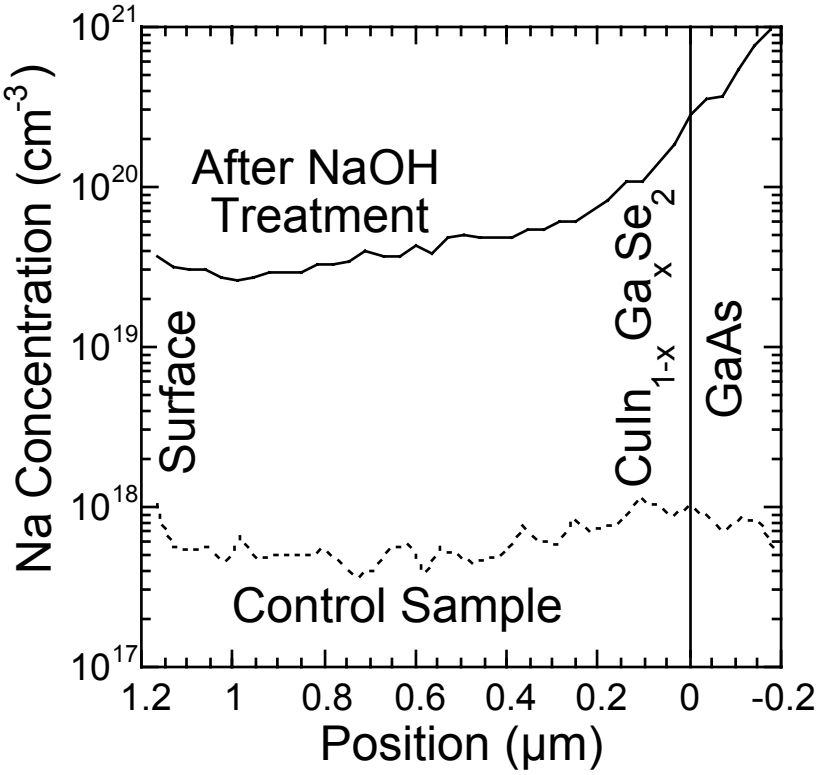

Figure II.D.ii.1: Na concentration as a function of depth for sample 135 comparing the control sample with the sample treated with NaOH. Nearly identical behaviors (qualitatively and quantitatively) were found in samples 150 and 152, not shown, for both treated and untreated samples.

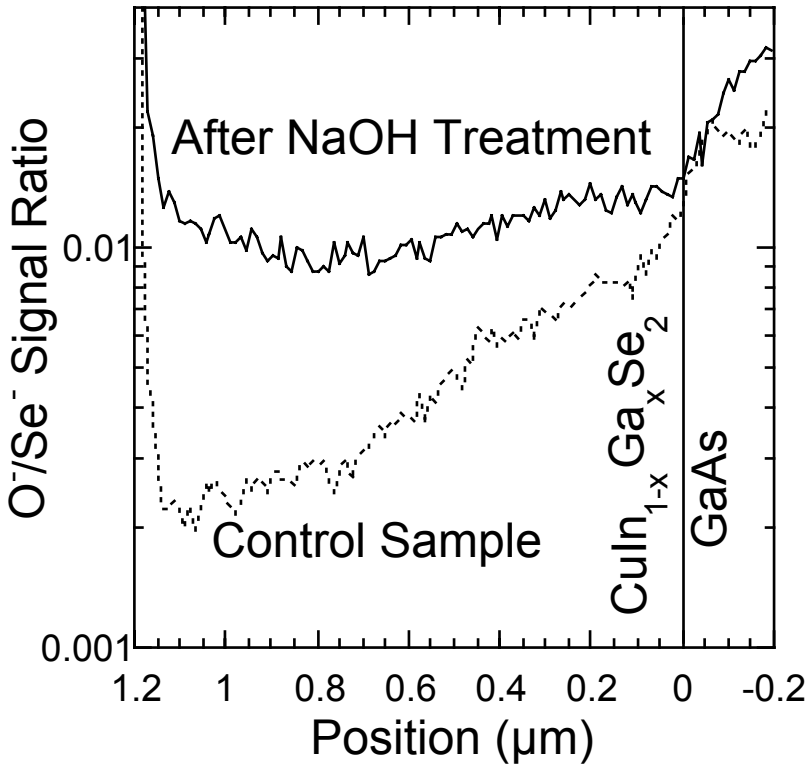

Figure II.D.ii.2: O^-/Se^- signal intensity ratio as a function of depth for sample 135 comparing the control sample with the sample treated with NaOH. No change in oxygen content was found in samples 150 and 152.

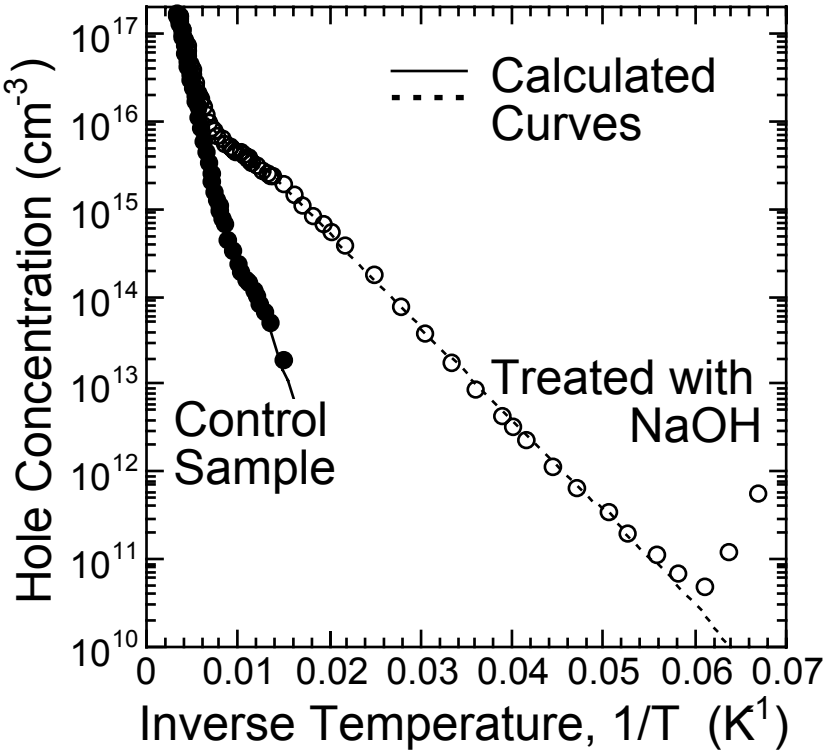

Figure II.D.ii.3: Measured and calculated carrier concentration vs. inverse temperature for a sample doped with Na using NaOH and a control portion of the same sample.

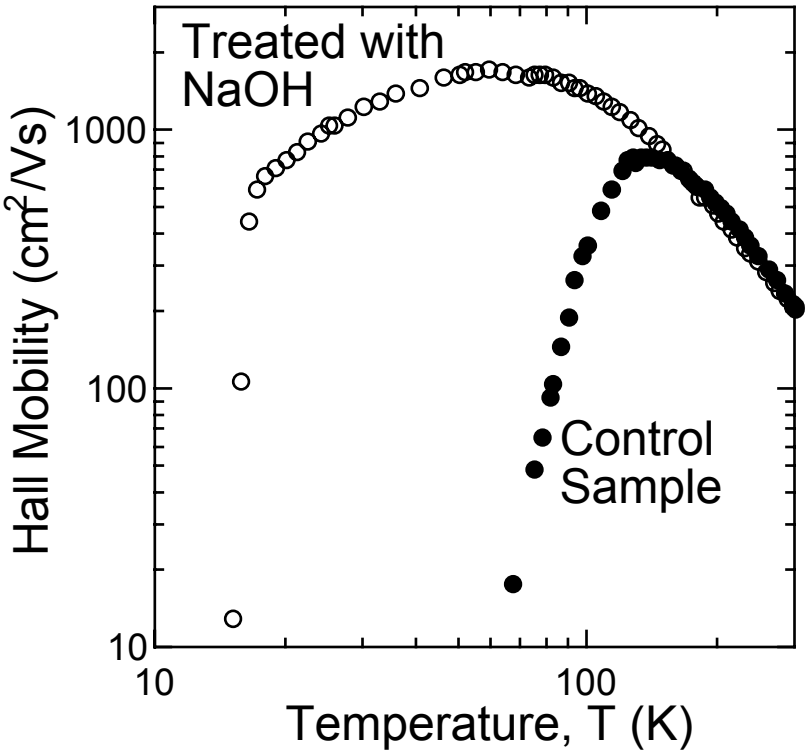

Figure II.D.ii.4: Hall mobility vs. temperature for a sample doped with Na using NaOH and a control portion of the same sample.

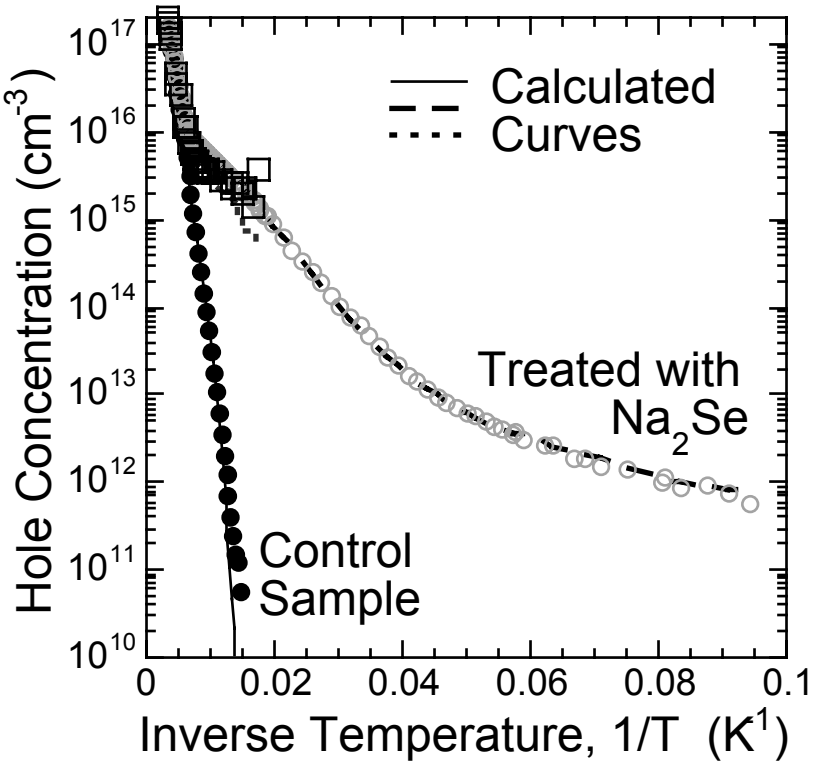

Figure II.D.ii.5: Measured and calculated carrier concentration vs. inverse temperature for two samples doped with Na using Na_2Se and the control sample (open circles). The treated samples were annealed at 550°C (filled diamonds) and 600°C (open squares).

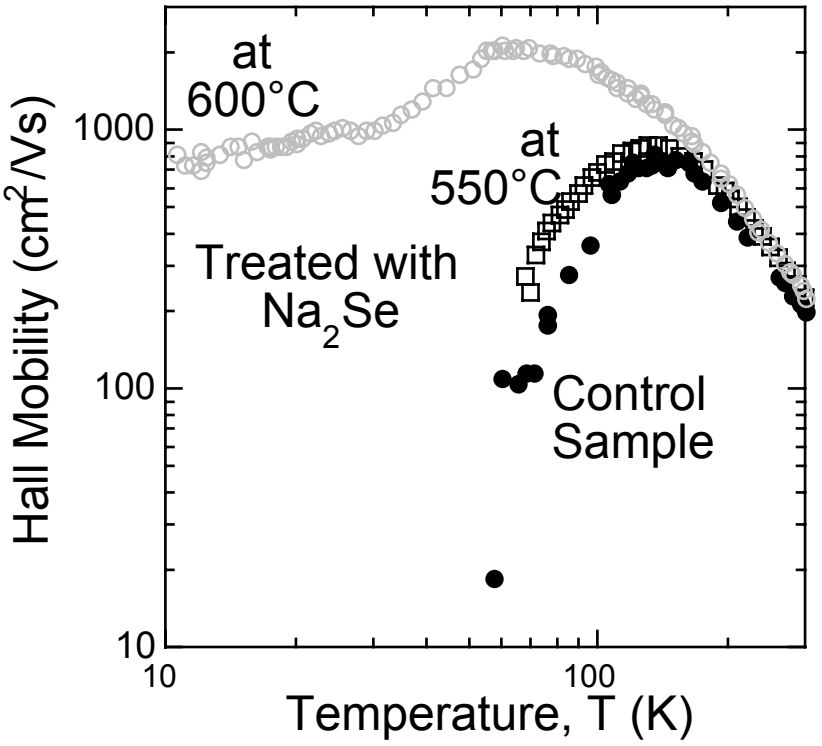

Figure II.D.ii.6: Hall mobility vs. temperature for two samples doped with Na using Na_2Se and an annealed but undoped control portion of the same sample (open circles). The treated samples were annealed at 550°C (filled diamonds) and 600°C (open squares).

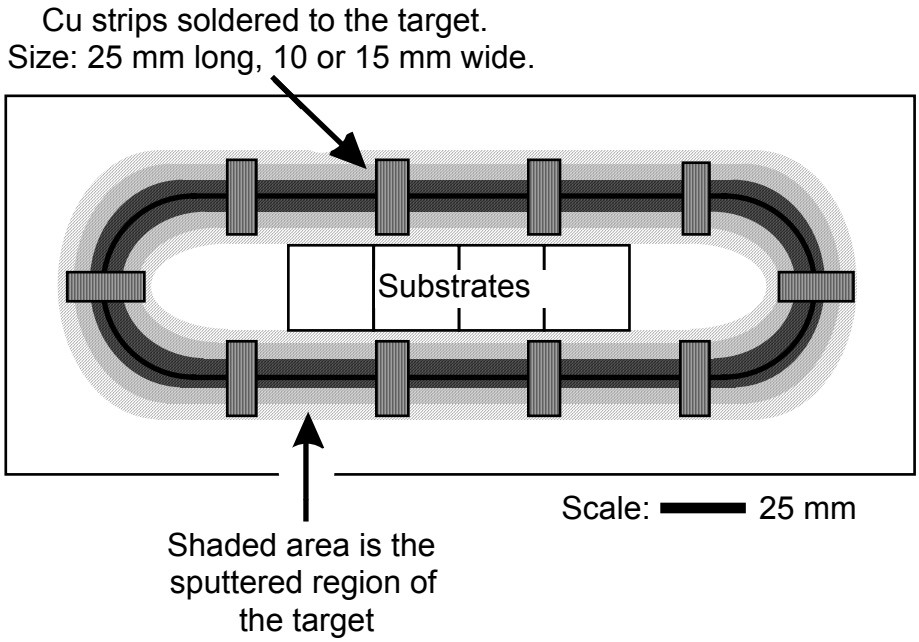

Figure 1. A schematic diagram of the arrangement of Cu foil attached to the Mo target.

Figure 2. X-ray diffraction spectra for two $Cu_{0.3}Mo_{0.7}$ films. Peaks are labeled according to the phase from which they arose. The unlabeled peaks were due to the Al substrate holder of the X-ray diffraction system.

Figure 3. TEM micrographs showing the microstructure of (a) an as-deposited and (b) an annealed (450°C, 60 min) $Cu_{0.3}Mo_{0.7}$ film. Transmission electron diffraction patterns for each layer are shown in the insets. The rings in the patterns were indexed from smallest to largest as follows. For the as-deposited layer: Mo (110), (200), (211), and (220). For the annealed layer: "X", Mo (110), Cu (111), Cu (200), Mo (200), "Y", Mo (211), Cu (220), Mo (220), and Cu (311), where rings "X" and "Y" are due to an unidentified phase, probably of bcc structure.

Figure 4. A cross sectional fractograph of a slightly Cu-rich CIS layer formed on a $Cu_{0.3}Mo_{0.7}$ metallization by exposure to a flux consisting of only In and Se.

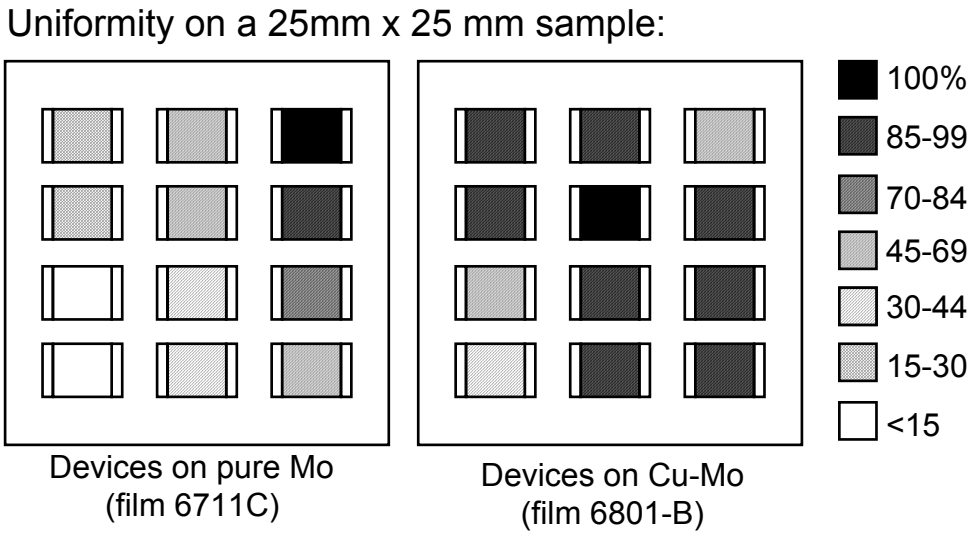

Figure 5. Comparison of the relative performances of solar cells on 25 x 25 mm substrates as a percentage of the efficiency of the best device on each substrate. The best performances are 8.4% on Mo and 10.0% on Cu-Mo.

REPORT DOCUMENTATION PAGE

Form Approved
OMB NO. 0704-0188

1. AGENCY USE ONLY (Leave blank)	2. REPORT DATE	3. REPORT TYPE AND DATES COVERED
	September 1999	Final Report, 28 June 1993 – 30 June 1998

4. TITLE AND SUBTITLE
Fundamental Studies of the Effect of Crystal Defects on $CuInSe_2$/CdS Heterojunction Behavior; Final Report, 28 June 1993 – 30 June 1998

5. FUNDING NUMBERS
C: XAD-3-12114-1
TA: PV902602

6. AUTHOR(S)
A. Rockett

7. PERFORMING ORGANIZATION NAME(S) AND ADDRESS(ES)
Department of Materials Science and Engineering
1-107 ESB, University of Illinois
1101 W. Springfield Ave
Urbana, IL 61801

8. PERFORMING ORGANIZATION REPORT NUMBER

9. SPONSORING/MONITORING AGENCY NAME(S) AND ADDRESS(ES)
National Renewable Energy Laboratory
1617 Cole Blvd.
Golden, CO 80401-3393

10. SPONSORING/MONITORING AGENCY REPORT NUMBER
SR-590-25623

11. SUPPLEMENTARY NOTES
NREL Technical Monitor: R.D. McConnell

12a. DISTRIBUTION/AVAILABILITY STATEMENT
National Technical Information Service
U.S. Department of Commerce
5285 Port Royal Road
Springfield, VA 22161

12b. DISTRIBUTION CODE

13. ABSTRACT *(Maximum 200 words)*

This report describes the work performed by the University of Illinois at Urbana-Champaign. The following results were obtained under the work funded by this subcontract.

Point defects and electronic properties of $Cu(In_{1-x}Ga_x)Se_2$:

- New record results for hole mobilities in $Cu(In_{1-x}Ga_x)Se_2$ based on single crystals grown by Rockett's group.
- Demonstrated the role of Ga in determining hole concentrations. Showed that Ga does not affect the hole mobility in this material and why this is the case. Determined the diffusion coefficient for Ga in single-crystal $Cu(In_{1-x}Ga_x)Se_2$.
- Demonstrated the structure and optoelectronic properties of the $CuIn_3Se_5$ ordered-defect phase of $CuInSe_2$.
- Characterized the detailed effects of Na on $Cu(In_{1-x}Ga_x)Se_2$ solar cells and on the fundamental properties of the material itself (reduces compensating donors in p-type materials).
- In collaboration with groups at the Universities of Salford and Liverpool in the United Kingdom, studied the effect of ion implantation damage on $Cu(In_{1-x}Ga_x)Se_2$ single-crystals.

Materials for and characterization of devices:

- Developed a novel contact metallurgy that improves adhesion to the underlying Mo back-contact in solar cells made with $Cu(In_{1-x}Ga_x)Se_2$. This material has also yielded substantial novel materials science behaviors, including grain rotation and growth prior to phase separation in a metastable binary alloy.
- Characterized the electroluminescence as a function of temperature and Ga content in $Cu(In_{1-x}Ga_x)Se_2$ solar cells and showed that the radiative recombination pathways are not band-to-band as in normal semiconductors, but rather, proceed through defect states.
- Working with a group at the University of Uppsala in Sweden, demonstrated novel aspects of the bonding and chemistry of dip-coated CdS heterojunction materials used as heterojunction partner materials in $Cu(In_{1-x}Ga_x)Se_2$ solar cells.

14. SUBJECT TERMS
photovoltaics ; crystal defects ; $CuInSe_2$; CdS ; grain boundaries ; heterojunction behavior ; stoichiometry ; point defects

15. NUMBER OF PAGES

16. PRICE CODE

17. SECURITY CLASSIFICATION OF REPORT	18. SECURITY CLASSIFICATION OF THIS PAGE	19. SECURITY CLASSIFICATION OF ABSTRACT	20. LIMITATION OF ABSTRACT
Unclassified	Unclassified	Unclassified	UL